

Dynamo effect in unstirred self-gravitating turbulence

Axel Brandenburg^{1,2,3,4*} and Evangelia Ntormousi^{5,6}

¹*Nordita, KTH Royal Institute of Technology and Stockholm University, Hannes Alfvéns väg 12, SE-10691 Stockholm, Sweden*

²*The Oskar Klein Centre, Department of Astronomy, Stockholm University, AlbaNova, SE-10691 Stockholm, Sweden*

³*McWilliams Center for Cosmology and Department of Physics, Carnegie Mellon University, 5000 Forbes Ave, Pittsburgh, PA 15213, USA*

⁴*School of Natural Sciences and Medicine, Ilia State University, 3-5 Cholakashvili Avenue, 0194 Tbilisi, Georgia*

⁵*Scuola Normale Superiore, Piazza dei Cavalieri 7, I-56126 Pisa, Italy*

⁶*Institute of Astrophysics, Foundation for Research and Technology-Hellas, Vasilika Vouton, GR-70013 Heraklion, Greece*

15 March 2022

ABSTRACT

In many astrophysical environments, self-gravity can generate kinetic energy, which, in principle, is available for driving dynamo action. Using direct numerical simulations, we show that in unstirred self-gravitating subsonic turbulence with helicity and a magnetic Prandtl number of unity, there is a critical magnetic Reynolds number of about 25 above which the work done against the Lorentz force exceeds the Ohmic dissipation. The collapse itself drives predominantly irrotational motions that cannot be responsible for dynamo action. We find that, with a weak magnetic field, one-third of the work done by the gravitational force goes into compressional heating and the remaining two-thirds go first into kinetic energy of the turbulence before a fraction of it is converted further into magnetic and finally thermal energies. Close to the collapse, however, these fractions change toward 1/4 and 3/4 for compressional heating and kinetic energy, respectively. When the magnetic field is strong, the compressional heating fraction is unchanged. Out of the remaining kinetic energy, one quarter goes directly into magnetic energy via work against the Lorentz force. The fraction of vortical motions diminishes in favor of compressive motions that are almost exclusively driven by the Jeans instability. For an initially uniform magnetic field, field amplification at scales larger than those of the initial turbulence are driven by tangling.

Key words: dynamo — MHD — turbulence — ISM: general

1 INTRODUCTION

Dynamo action describes the conversion of kinetic energy into magnetic (Moffatt 1978). This can also happen under non-stationary conditions, for example in decaying turbulence, where the kinetic energy tends to decay in power-law fashion, so the growth of the magnetic field is no longer exponential in time, as it would be in stationary turbulence (Brandenburg et al. 2019; Sur 2019). This type of unsteady energy conversion is expected to play a role in many astrophysical settings where the magnetic Reynolds number is high enough.

In the interstellar medium (ISM), as well as on cosmological scales, self-gravity can be the dominant driver of turbulence (Field et al. 2008; Klessen & Hennebelle 2010). In the context of galaxy growth, the gas accretion flows typically predicted by numerical simulations around galactic disks (Dekel et al. 2009; Nelson et al. 2015, for some examples) convert gravitational potential energy into kinetic energy. In the ISM of galaxies, the gravitational instability of the disk itself has been proposed as the main source of turbulence (e.g., Bournaud et al. 2010; Krumholz & Burkhardt

2016), with a contribution that can be as strong as that of supernova (SN) feedback (Krumholz et al. 2018). Finally, gravitational accretion is believed to be the main driver of turbulence within molecular clouds (Ibáñez-Mejía et al. 2017).

While the exact fraction of potential energy that goes into turbulence is unknown – and probably depends strongly on the environment – it is clear that, in general, self-gravity can be an important source of kinetic energy. This kinetic energy can, in turn, be converted into magnetic energy through dynamo action. Earlier work has shown that in gravitationally unstable flows, the magnetic energy increases during the linear phase of the collapse, and that the magnetic energy declines during the nonlinear phase of the dynamo (Sur et al. 2010, 2012; Xu & Lazarian 2020).

The kinematic phase of a turbulent dynamo within a collapsing cloud was considered by Federrath et al. (2011b), who reported exponential growth of the magnetic field with a Kazantsev spectrum, as was previously found for forced turbulence. Their dynamo growth rate exceeded the collapse rate, provided their resolution criterion of 30 grid cells per Jeans length is obeyed at any position in space and any point in time. As they demonstrated, at lower resolution, the magnetic field is only amplified because of flux freezing.

Magnetic fields can also be produced by tangling of a large-

* E-mail: brandenb@nordita.org

scale seed. This type of growth can still occur in two dimensions, where true dynamo action is impossible according to the Cowling antidynamo theorem; see [Hide & Palmer \(1982\)](#) for a generalized antidynamo theorem relevant to compressible flows.

An important goal of this work is to characterize dynamo action in unstirred decaying turbulence, where gravity provides an energy source that can eventually revert the decay of the turbulence. We approach the question with direct numerical simulations of systems with different turbulent initial conditions, and in various degrees of gravitational instability. Our turbulent initial conditions are almost exclusively subsonic with a Mach number of 0.2. One motivation behind this choice is that the critical magnetic Reynolds number for dynamo action increases by about a factor of two when the flow is supersonic ([Haugen et al. 2004b](#)). The low initial Mach number also allows us to focus on any dynamo action triggered by the collapse-produced turbulence, rather than by the decaying turbulence from the initial conditions. In fact, we will show that, as the models evolve, the collapse itself produces turbulence that eventually dominates the initial flow. However, since turbulence in many astrophysical environments, such as molecular clouds, is supersonic ([Schneider et al. 2013](#)), we will also present one run with an initial Mach number of two. Furthermore, given that the sonic Mach number is scale-dependent ([Federrath et al. 2021](#)), our early subsonic phase might still be applicable to correspondingly small scales.

In driven turbulence, dynamo action can be adequately characterized by the growth rate, evaluated as the time derivative of the root-mean-square (rms) magnetic field. In stationary conditions, this quantity stays reasonably constant with time. However, in the non-stationary conditions that we study here, namely decaying turbulence and turbulence generated by gravitational collapse, the magnetic field no longer grows exponentially, and the growth rate cannot be used as a dynamo criterion. Therefore, in this study we explore new, more general dynamo criteria that allow for non-stationary turbulence conditions. We decided to base our dynamo criterion on the work against the Lorentz force, where the magnetic curvature force plays the dominant role. When this work exceeds the Joule dissipation, it might be a dynamo. This definition of a possible dynamo agrees with the standard definition of a positive growth rate when the flow is steady, but, unlike any dynamo criterion proposed so far, it can easily be applied to unsteady flows. It does not, however, distinguish dynamos in three dimensions from just temporary amplification through tangling and compression, as can be seen, for example, in two dimensions. To exclude the effects of two-dimensional (2-D) compression or tangling, we propose splitting the Lorentz work term into two contributions, of which one is absent in 2-D. This leads to an additional criterion that must be satisfied for dynamo action.

We use high-resolution numerical simulations with fixed kinematic viscosity and magnetic diffusivity to be able to define the threshold for dynamo action. Note also that, unlike codes with adaptive mesh refinement, where the accuracy of the solution varies in space (see, for example, [Federrath et al. 2010](#)), we resolve all regions in space equally well. There should therefore be no doubt that our velocity spectra and other diagnostics are representative of the domain as a whole.

In this paper, we first define our model (Sect. 2). We then

present the results for the energy spectra and the energy conversion rates, as well as characteristic wavenumbers and dynamo excitation conditions for weak initial magnetic fields (Sect. 3). We then compare our results with those for strong initial magnetic fields (Sect. 4), and conclude in Sect. 5.

2 THE MODEL

2.1 Governing equations

We consider an isothermal gas with sound speed c_s in a cubic periodic domain of size L^3 , so the smallest wavenumber is $k_1 = 2\pi/L$. The pressure is given by $p = \rho c_s^2$, where ρ is the density. The governing equations are ([Passot et al. 1995](#))

$$\nabla^2 \Phi = 4\pi G (\rho - \rho_0), \quad (1)$$

$$\frac{D\mathbf{u}}{Dt} = -\nabla (c_s^2 \ln \rho + \Phi) + \frac{1}{\rho} (\mathbf{J} \times \mathbf{B} + \nabla \cdot 2\nu \mathbf{S}), \quad (2)$$

$$\frac{D \ln \rho}{Dt} = -\nabla \cdot \mathbf{u}, \quad (3)$$

$$\frac{\partial \mathbf{A}}{\partial t} = \mathbf{u} \times \mathbf{B} - \eta \mu_0 \mathbf{J}, \quad (4)$$

where Φ is the gravitational potential, G is Newton's constant, ρ_0 is the spatially averaged density, which is constant in time because of mass conservation, \mathbf{u} is the velocity, $\mathbf{J} = \nabla \times \mathbf{B} / \mu_0$ is the current density, μ_0 is the vacuum permeability, $\mathbf{B} = \nabla \times \mathbf{A}$ is the magnetic field in terms of the magnetic vector potential, $S_{ij} = \frac{1}{2}(u_{i,j} + u_{j,i}) - \frac{1}{3}\delta_{ij} \nabla \cdot \mathbf{u}$ are the components of the rate-of-strain tensor with commas denoting partial derivatives, and ν is the kinematic viscosity.

The occurrence of the constant ρ_0 in Eq. (1) comes from a change of coordinates to a comoving reference frame that is following the global expansion of the background medium (see [Alecian & Leorat 1988](#)). This is a consequence of working with an infinite (unbounded) medium. Such a medium can be stationary, but not static. This was also explained by [Falco et al. \(2013\)](#), who clarified why the famous Jeans swindle ([Binney & Tremaine 2008](#)) actually works. In this accelerated frame, Eqs. (1)–(4) describe the departure of collapsing structures from the background flow.

Linearizing Eqs. (1)–(3) around $\rho = \rho_0$ and $\mathbf{u} = 0$, and assuming the perturbations to be proportional to $e^{i\mathbf{k}\cdot\mathbf{x} + \sigma t}$ yields the dispersion relation $\sigma^2 = \sigma_J^2 - c_s^2 k^2$, where $\sigma_J^2 = 4\pi G \rho_0$ with σ_J being the gravitational or Jeans growth rate ([Jeans 1902](#)). The pressureless free-fall time is $t_{\text{ff}} = \sqrt{3/8} \pi / \sigma_J \approx 1.92 / \sigma_J$ ([Shu 1992](#)). The Jeans wavenumber is $k_J = \sigma_J / c_s$, and the Jeans length is then $\lambda_J = 2\pi / k_J$ (see, e.g., [Bonazzola et al. 1987](#); [Truelove et al. 1997](#)). According to the classical Jeans criterion for gravitational instability, an interstellar gas cloud will collapse if its free-fall time is shorter than the sound crossing time in its interior, or, more specifically, $t_{\text{ff}} c_s k_1 < 1.92$.

2.2 Diagnostic quantities

2.2.1 Energetics

Throughout this paper, we use periodic boundary conditions, so all surface integrals vanish and no mass is lost. In

the following, volume averages are denoted by angle brackets. It is instructive to inspect the evolution equations of mean potential, kinetic, and magnetic energy densities, $\mathcal{E}_P = -\langle(\nabla\Phi)^2\rangle/8\pi G$, $\mathcal{E}_K = \langle\rho_0\mathbf{u}^2\rangle/2$, and $\mathcal{E}_M = \langle\mathbf{B}^2\rangle/2\mu_0$, respectively (Banerjee & Kritsuk 2018). They are given by

$$\frac{d\mathcal{E}_P}{dt} = -W_J, \quad (5)$$

$$\frac{d\mathcal{E}_K}{dt} = W_P + W_J + W_L - Q_K, \quad (6)$$

$$\frac{d\mathcal{E}_M}{dt} = -W_L - Q_M, \quad (7)$$

where $W_P = -\langle\mathbf{u} \cdot \nabla p\rangle = \langle p \nabla \cdot \mathbf{u}\rangle$ is the work done by the pressure force, $W_J = -\langle\rho\mathbf{u} \cdot \nabla\Phi\rangle$ is the work done by the gravity term, $W_L = \langle\mathbf{u} \cdot (\mathbf{J} \times \mathbf{B})\rangle$ is the work done by the Lorentz force, and $Q_K = \langle 2\rho\nu\mathbf{S}^2\rangle$ and $Q_M = \langle\mu_0\eta\mathbf{J}^2\rangle$ are the viscous and Joule dissipation terms. The thermal energy density is sourced by the terms $-W_P + Q_K + Q_M$, but with the employed isothermal equation of state, the thermal energy density is not evolved.

The work done by the gravity term ($W_J > 0$) leads to a decrease of the potential energy density and to an increase in the kinetic energy density. During the collapse, the virial parameter $\alpha_{\text{vir}} = 2\mathcal{E}_K/|\mathcal{E}_P|$ is expected to be around unity, but this expectation can be different at large Mach numbers (Ntormousi & Hennebelle 2019) and for strong magnetic fields; see Federrath & Klessen (2012), who also emphasize the difference between periodic setups, such as ours, and isolated spheres.

We have defined all work terms such that they enter with a plus sign in Eq. (6), i.e., they lead to an increase in the kinetic energy density if they are positive, and thus to a loss in some other energy reservoir. As noted above, a positive W_J term leads to a loss of potential energy. Likewise, a positive W_P term leads to a loss in thermal energy. Gravitational collapse however, leads to compressional heating and W_P is therefore negative. Furthermore, dynamo action leads to a growth in magnetic energy if W_L is negative.

The W_L term can be split into three constituents: $W_L^c = -\langle\mathbf{u} \cdot \nabla\mathbf{B}^2/2\mu_0\rangle$, $W_L^\parallel = \langle\mathbf{u} \cdot (\mathbf{B} \cdot \nabla\mathbf{B}/\mu_0)_\parallel\rangle$, and $W_L^\perp = \langle\mathbf{u} \cdot (\mathbf{B} \cdot \nabla\mathbf{B}/\mu_0)_\perp\rangle$. Here, $-\nabla\mathbf{B}^2/2\mu_0$ is the magnetic pressure contribution of $\mathbf{J} \times \mathbf{B}$, and $(\mathbf{B} \cdot \nabla\mathbf{B}/\mu_0)_\parallel$ and $(\mathbf{B} \cdot \nabla\mathbf{B}/\mu_0)_\perp$ are the stretching terms along and perpendicular to the magnetic field. The last two forces are also referred to as tension and curvature forces; see Nordlund et al. (1992) for their contributions to a convective dynamo.

In the following, we also decompose W_L by writing it as $W_L = -\langle\mathbf{J} \cdot (\mathbf{u} \times \mathbf{B})\rangle$ and expanding the curl to get

$$-\langle\mathbf{J} \cdot (\mathbf{u} \times \mathbf{B})\rangle = \langle J_i u_j (A_{i,j} - A_{j,i}) \rangle \equiv W_L^{2D} + W_L^{3D}. \quad (8)$$

Here, we make use of the fact that the Weyl gauge has been used in Eq. (4). In two dimensions, the magnetic field can be represented as $\mathbf{B} = \nabla \times A_z \hat{\mathbf{z}}$, with its x and y components lying in the xy plane. Then the term $W_L^{3D} = -\langle J_i u_j A_{j,i} \rangle$ vanishes in 2-D. Thus, we can identify W_L^{3D} with a contribution that characterizes the 3-D nature of the system and can therefore be a proxy for dynamo action, provided W_L^{3D} is large enough.

To characterize the flow of energy, it is convenient to define the fractions $\epsilon_J^P \equiv -W_P/W_J$, $\epsilon_J^L \equiv -W_L/W_J$, $\epsilon_J^{+K} \equiv$

$\dot{\mathcal{E}}_K/W_J$, and $\epsilon_J^{-K} = Q_K/W_J$. Likewise, we define the fractions $\epsilon_L^{+M} \equiv \mathcal{E}_M/(-W_L)$, and $\epsilon_J^{-M} = Q_M/(-W_L)$. To characterize the growth or decay of the magnetic field, we define the nondimensional ratio $\epsilon_M^\Delta = (-W_L - Q_M)/Q_M$. A related quantity is the pseudo (or instantaneous) growth rate of magnetic energy, $\gamma = (-W_L - Q_M)/\mathcal{E}_M$, which can be divided into the contributions $\gamma_c + \gamma_\parallel + \gamma_\perp = \gamma$ from compression and stretching parallel and perpendicular to the magnetic field, where $\gamma_\perp = (-W_L^\perp - Q_M)/\mathcal{E}_M$ will play the most important role, and $\gamma_c = -W_L^\parallel/\mathcal{E}_M$ and $\gamma_\parallel = -W_L^c/\mathcal{E}_M$ contribute either later or in the presence of strong initial magnetic fields. Likewise, we define $\gamma_{2D} = -(W_L^{2D} + Q_M)/\mathcal{E}_M$ and $\gamma_{3D} = -W_L^{3D}/\mathcal{E}_M$, so that $\gamma_{2D} + \gamma_{3D} = \gamma$.

2.2.2 Characteristic wavenumbers

To characterize the compressive and solenoidal flow components, it is convenient to compute the rms velocity divergence, $(\nabla \cdot \mathbf{u})_{\text{rms}} = \langle(\nabla \cdot \mathbf{u})^2\rangle^{1/2}$, and the rms vorticity, $\omega_{\text{rms}} = \langle\omega^2\rangle^{1/2}$, where $\omega = \nabla \times \mathbf{u}$, and to define

$$k_{\nabla \cdot \mathbf{u}} = (\nabla \cdot \mathbf{u})_{\text{rms}}/u_{\text{rms}}, \quad (9)$$

$$k_\omega = \omega_{\text{rms}}/u_{\text{rms}}, \quad (10)$$

which have the dimension of a wavenumber. Since the flow is helical, we can also define the wavenumber

$$k_{\omega \cdot \mathbf{u}} = |(\omega \cdot \mathbf{u})|/u_{\text{rms}}^2, \quad (11)$$

which characterizes the typical wavenumber where helicity plays a role. Large values of $k_{\nabla \cdot \mathbf{u}}$, k_ω , and $k_{\omega \cdot \mathbf{u}}$ imply strong flow divergences or compressions, strong vortices, and strong swirls, respectively. To characterize the flow compression from the gravitational collapse, we also define

$$k_{p\nabla \cdot \mathbf{u}} = -\langle p \nabla \cdot \mathbf{u} \rangle / p_0 u_{\text{rms}} \quad (\text{when } k_{p\nabla \cdot \mathbf{u}} > 0), \quad (12)$$

where $p_0 = \rho_0 c_s^2$ has been introduced for brevity. The relevance of $k_{p\nabla \cdot \mathbf{u}}$ to the collapse phenomenon is motivated by the fact that a strong flow compression or flow convergence ($\nabla \cdot \mathbf{u} < 0$) correlates with pressure (defined in the beginning of Sect. 2.1). Indeed, it turns out that $k_{p\nabla \cdot \mathbf{u}}$ is very small prior to collapse, but it approaches $k_{\nabla \cdot \mathbf{u}}$ close to the collapse.

2.2.3 Spectra

We define the kinetic and magnetic energy spectra, $E_K(k, t)$ and $E_M(k, t)$, respectively. They are normalized such that $\int E_K(k, t) dk = \mathcal{E}_K$ and $\int E_M(k, t) dk = \mathcal{E}_M$. It can be advantageous to express them as wavenumber-dependent Reynolds and Lundquist numbers by defining a velocity and a magnetic field,

$$u_k(t) = \sqrt{2kE_K(k, t)/\rho_0}, \quad B_k(t) = \sqrt{2\mu_0 kE_M(k, t)}, \quad (13)$$

respectively. We then define

$$\text{Re}_k(t) = u_k(t)/\nu k \quad \text{and} \quad \text{Lu}_k(t) = B_k(t)/(\sqrt{\mu_0 \rho_0} \eta k). \quad (14)$$

A Kolmogorov-type spectrum with $E_K(k) \propto k^{-5/3}$ corresponds then to $u_k \propto k^{-1/3}$ and $\text{Re}_k \propto k^{-4/3}$. In the following, we also quote these values at $k = k_t$, where the initial kinetic energy spectrum peaks. We also define the Reynolds number

Re_t based on the actual rms velocity, with Re_{t^*} denoting the value at the time t^* , when the exponentially growing gas motions from the Jeans instability begin to dominate over the initial turbulence. In the present normalization, the values of Re_{k_f} and Re_t are close to the Taylor microscale Reynolds number (Tennekes & Lumley 1972), which is universally defined as $Re_\lambda = v' \lambda_{\text{Tay}} / \nu$. Here, $v' = u_{\text{rms}} / \sqrt{3}$ is the one-dimensional rms velocity and $\lambda_{\text{Tay}} = \sqrt{15 \nu \rho_0 / Q_K} v'$ is the Taylor microscale.

Kinetic and magnetic helicity spectra, $H_K(k, t)$ and $H_M(k, t)$, are normalized such that $\int H_K(k, t) dk = \langle \boldsymbol{\omega} \cdot \mathbf{u} \rangle$ and $\int H_M(k, t) dk = \langle \mathbf{A} \cdot \mathbf{B} \rangle$ are the mean kinetic and magnetic helicities. They obey the realizability conditions $|H_K(k)| \leq 2kE_K(k)$ and $|H_M(k)| \leq (2/k)E_M(k)$ (Moffatt 1978). It is then convenient to plot the relative helicities given by the corresponding ratios $H_K(k)/2kE_K(k)$ and $kH_M(k)/2E_M(k)$, respectively.

We also plot the enstrophy and logarithmic density spectra, $E_\omega(k)$ and $E_{\ln \rho}(k)$, respectively. They are normalized such that $\int E_\omega(k) dk = \langle \boldsymbol{\omega}^2 \rangle / 2$ and $\int E_{\ln \rho}(k) dk = \langle (\ln \rho)^2 \rangle$. Here, $E_\omega(k)/k^2$ corresponds to the kinetic energy spectrum of the vortical part of the velocity, and $E_\rho(k)$ reflects its irrotational part. Finally, the potential energy spectrum is normalized such that $\int E_P(k) dk = \mathcal{E}_P$.

2.3 Units and parameters

In the plots shown in this paper, we express velocities in units of c_s , lengths in units of k_1^{-1} (defined in the beginning of Sect. 2.1), density in units of ρ_0 , and the magnetic field in units of $\sqrt{\mu_0 \rho_0} c_s$. In practice, we do this by choosing in our simulations $c_s = k_1 = \rho_0 = \mu_0 = 1$. In the following, to remind the readers, we often include relevant combinations of c_s and k_1 when specifying the numerical values, but in other cases, especially in the table entries, we simply omit them to avoid lengthy notation.

Since we do not invoke cooling or any other processes that depend on dimensions, our simulations can be scaled to any arbitrary system by choosing physical values for c_s , k_1 , and ρ_0 . To illustrate the normalization used in the simulations, let us consider, as an example, the case $c_s = 1 \text{ km s}^{-1}$ and $k_1 = 1 \text{ pc}^{-1}$. Then, our time unit is $(c_s k_1)^{-1} = 0.98 \text{ Myr}$, so we can think of our normalized time as 1 Myr. Considering a typical density of $\rho_0 = 10^{-21} \text{ g cm}^{-3}$ for the dense regions of the ISM, we have $\sigma_J^{-1} = 1.1 \text{ Myr}$, or $t_{\text{ff}} = 2.1 \text{ Myr}$. Then, the corresponding Jeans wavenumber is $k_J = 0.9 \text{ pc}^{-1}$, so the Jeans length is $\lambda_J = 7 \text{ pc}$. For $k_1 = 1 \text{ pc}^{-1}$, the side length of the computational domain is $6.28 \text{ pc} \approx 0.9 \lambda_J$. The corresponding normalized (nondimensional) quantities are then $\sigma_J^{-1} c_s k_1 = 1.1$ and $\sigma_J / c_s k_1 = k_J / k_1 = 0.9$. All work terms are given in units of $\rho_0 c_s^3 k_1$, which corresponds to $1 \text{ g cm}^{-3} (\text{km s}^{-1})^3 / \text{pc} = 10^{-11} \text{ erg cm}^{-3} \text{ Myr}^{-1}$ or $0.0024 L_\odot \text{ pc}^{-3}$. In this work, we choose two values for $\sigma_J / c_s k_1$, 2 and 5, which means that our computational domain is two or five Jeans lengths long, and our mesh of 2048^3 cells resolves the Jeans length initially with 1024 or 410 points, respectively. As the collapse proceeds, the maximum density increases and the nominal Jeans length decreases. To stay within the resolution criterion of Federrath et al. (2011b) of 30 mesh points per Jeans length, we can only trust the time before the maximum density has exceeded the initial

value by a factor of $(1024/30)^2 \approx 1200$ and $(410/30)^2 \approx 200$ for the cases with $\sigma_J / c_s k_1 = 2$ and 5, respectively.

As mentioned earlier, we focus on subsonic turbulence, where dynamo action is most easily obtained (Haugen et al. 2004b; Federrath et al. 2011a). In the context of molecular cloud contraction, this choice puts them in the regime of low-mass pre-stellar cores. While molecular clouds are supersonically turbulent on large scales, low-mass pre-stellar cores are subsonic (Larson 1981; Myers et al. 1991; André et al. 2007). Such weak motions could originate from the decay of larger-scale turbulence (e.g., Hennebelle & Falgarone 2012).

We choose the amplitude of the initial velocity field such that the initial Mach number $Ma = u_{\text{rms}} / c_s$ is around 0.1. The turnover time is given by $\tau = (u_{\text{rms}} k_f)^{-1}$. We are interested in the cases where the turnover time is comparable to or less than the free-fall time scale σ_J^{-1} , where σ_J must be larger than unity (in units of $c_s k_1$) for the Jeans instability to be excited. Given that $Ma \approx 0.1$, this automatically implies that $k_f / k_1 \geq 10$, provided that σ_J is not much larger than unity. We focus on the case with $\sigma_J = 5 c_s k_1$, but we have also experimented with smaller values of two and even 1.1. However, when σ_J is that small, it takes a long time for the instability to develop and by that time the initial turbulence would have decayed too much.

The magnetic field strength can also be specified in terms of $v_A^{\text{rms}} = B_{\text{rms}} / \sqrt{\mu_0 \rho_0}$. In the second part of the paper, we consider values of v_A^{rms} / c_s in the range 0.04–0.4. In the first part of the paper, however, we are interested in the kinematic regime and therefore consider values of around 10^{-18} . In all cases, we adopt a magnetic Prandtl number of unity, i.e., $\nu / \eta = 1$, so the Reynolds number is always equal to the magnetic Reynolds number.

2.4 Initial conditions

As initial conditions, we assume $\rho = \rho_0$, so there is no density perturbation. However, we assume that the velocity and magnetic fields have a random distribution with a k^4 spectrum below a given wavenumber k_f and a $k^{-5/3}$ spectrum above k_f . We assume the initial velocity to be maximally helical at all wavenumbers, but take the magnetic field to be nonhelical. This then leads to perturbations in the system that trigger the Jeans instability. Again, with a few exceptions, we deliberately choose a very weak initial magnetic field so as to see the possibility of a kinematic dynamo at early times. A dynamo effect in decaying turbulence has been found in an earlier study (Brandenburg et al. 2019), where one saw a significant temporal increase of the magnetic field over several orders of magnitude when the initial field is sufficiently weak, but no significant increase was found for fields that start off in near-equipartition with the turbulence.

2.5 Numerical simulations

We use the PENCIL CODE (Pencil Code Collaboration et al. 2021), which employs sixth order accurate derivatives in space and a third order accurate time stepping scheme. Self-gravity was implemented by Johansen et al. (2007) for modeling planetesimal formation and employs Fourier transformation. That same module is also being used for studying dust formation in the ISM (Mattsson & Hedvall 2022).

Table 1. Energy flux ratios and Reynolds numbers for the runs discussed in the paper. Here, k_J and k_f are in units of k_1 .

Run	k_J	k_f	Re_{k_f}	Re_{t_*}	Lu_{t_*}	ϵ_J^P	ϵ_J^{+K}	ϵ_J^{-K}	ϵ_J^L	ϵ_L^{+M}	ϵ_J^{-M}	ϵ_M^Δ	γ	N^3
O1	2	10	500	1000	2.3×10^{-13}	0.30	0.68	0.02	0.000	0.28	0.72	0.40	1.39	2048 ³
O2	5	2	100	1000	3.9×10^{-14}	0.32	0.67	0.01	0.000	0.49	0.51	0.96	0.83	1024 ³
A	5	10	500	1000	1.0×10^{-13}	0.33	0.64	0.03	0.000	0.35	0.65	0.70	3.0	2048 ³
B	5	10	100	200	9.9×10^{-15}	0.34	0.63	0.03	0.000	0.21	0.79	0.26	0.44	2048 ³
b	5	10	100	200	9.9×10^{-15}	0.31	0.66	0.03	0.000	0.20	0.76	0.32	0.54	1024 ³
C	5	10	20	40	9.6×10^{-16}	0.34	0.63	0.03	0.000	0.06	0.94	0.06	0.08	2048 ³
D	5	10	5	10	1.1×10^{-16}	0.31	0.66	0.03	0.000	-0.82	1.82	-0.48	-0.44	1024 ³
E	5	10	1	2	5.6×10^{-18}	0.25	0.73	0.02	0.000	-11.5	12.5	-0.96	-1.13	1024 ³
S	5	10	500	1300	8.7×10^{-14}	0.31	0.60	0.09	0.000	0.34	0.66	0.79	2.47	1024 ³
M1	5	10	500	1000	1.3×10^3	0.36	0.46	0.13	0.05	-17.6	18.6	-0.94	-0.38	2048 ³
M2	5	10	500	1000	6.4×10^2	0.31	0.67	0.01	0.01	-0.97	1.97	-0.45	-0.16	2048 ³
M3	5	10	500	1000	4.1×10^2	0.32	0.65	0.01	0.02	0.03	0.97	0.17	0.11	2048 ³
M4	5	10	100	200	9.8×10^0	0.33	0.65	0.02	0.00	0.20	0.80	0.25	0.42	2048 ³
I1	5	10	500	1000	1.6×10^3	0.29	0.68	0.01	0.02	0.67	0.33	2.63	0.05	2048 ³
I2	5	10	500	1000	7.5×10^2	0.31	0.67	0.01	0.01	0.20	0.80	0.26	0.03	2048 ³
I3	5	10	500	1000	4.3×10^2	0.32	0.65	0.01	0.02	0.32	0.68	0.60	0.33	2048 ³

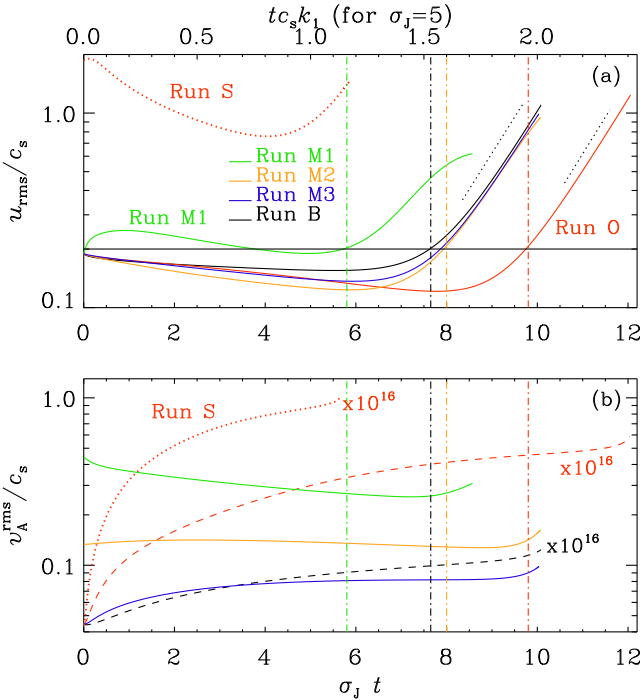


Figure 1. Mach numbers for (a) the rms velocity and (b) the rms Alfvén speed. The red and black dashed lines in (b) have been scaled up by 10^{16} to make them visible. The vertical dashed-dotted lines denote the times t_* when the Mach number has recovered to the original value of about 0.2. (For Run S, the initial value of 2 was not recovered before the collapse.) The dotted lines correspond to $\exp(\sigma t)$ with $\sigma = 0.9\sqrt{24}$ and $\sqrt{3}$, respectively. The upper abscissa gives time as $t c_s k_1$ for the cases with $\sigma_J/c_s k_1 = 5$.

Many of the diagnostic quantities are calculated during run time, including spectra and slices. Most of the secondary data that are used for the plots are publicly available; see the code and data availability statement at the end of the paper.

3 RESULTS FOR WEAK MAGNETIC FIELDS

3.1 Visualizations and spectra

In Figure 1 we show the evolution of the Mach number and the rms Alfvén speed normalized to the sound speed for $\sigma_J = 2c_s k_1$ (Run O1) and $5c_s k_1$ (Runs A–E), so $t_{ff} c_s k_1 = 0.96$ and 0.38, respectively. In both cases, an exponential growth of Ma commences at some time. For Run O1, the growth rate agrees with that expected from the dispersion relation, i.e., $\sigma/c_s k_1 = \sqrt{3}$, but for Run B, the actual value is 10% smaller than the theoretically expected value, $\sigma/c_s k_1 = \sqrt{24}$, which could be related to the finite viscosity. We define the moment when the rms velocity has recovered to its initial value (denoted by the horizontal line for $u_{\text{rms}}(0)/c_s = 0.2$) as t_* . Those characteristic times ($t_* c_s k_1 \approx 1.5$ and 4.9 for $\sigma_J/c_s k_1 = 5$ and 2, respectively) are denoted by vertical dashed-dotted lines in the corresponding colors. Those times correspond approximately to the moment when the negative potential energy density begins to exceed the kinetic energy density, i.e., when the virial parameter α_{vir} drops below two; see Appendix A for a demonstration. In the supersonic case of Run S, the collapse is found to occur earlier. This is mainly a consequence of the stronger initial perturbations (see, e.g. Mac Low & Klessen 2004, for a review).

The growth of the magnetic field is quantified by the ratio v_A/c_s ; see Appendix B for a comparison with other measures such as B_{rms} and the ratio $|\mathbf{B}|/\rho^{2/3}$. Given that the velocity is decaying during the first part of the evolution, we cannot expect an exponential growth of the magnetic field. During the second part, when the velocity is exponentially increasing, the magnetic field does not show a corresponding increase. In the following, we tentatively associate the slow growth of the magnetic field during the decay phase of the velocity field with a dynamo, and the second part, which is dominated by the Jeans instability, with just compressional amplification. With these observations in mind, we continue using the term dynamo, but leave it for further analysis to establish more rigorous and convincing criteria.

For the rest of the paper, we focus on the case $\sigma_J = 5c_s k_1$, so we expect growth for $k < k_J \equiv 5k_1$. We summarize

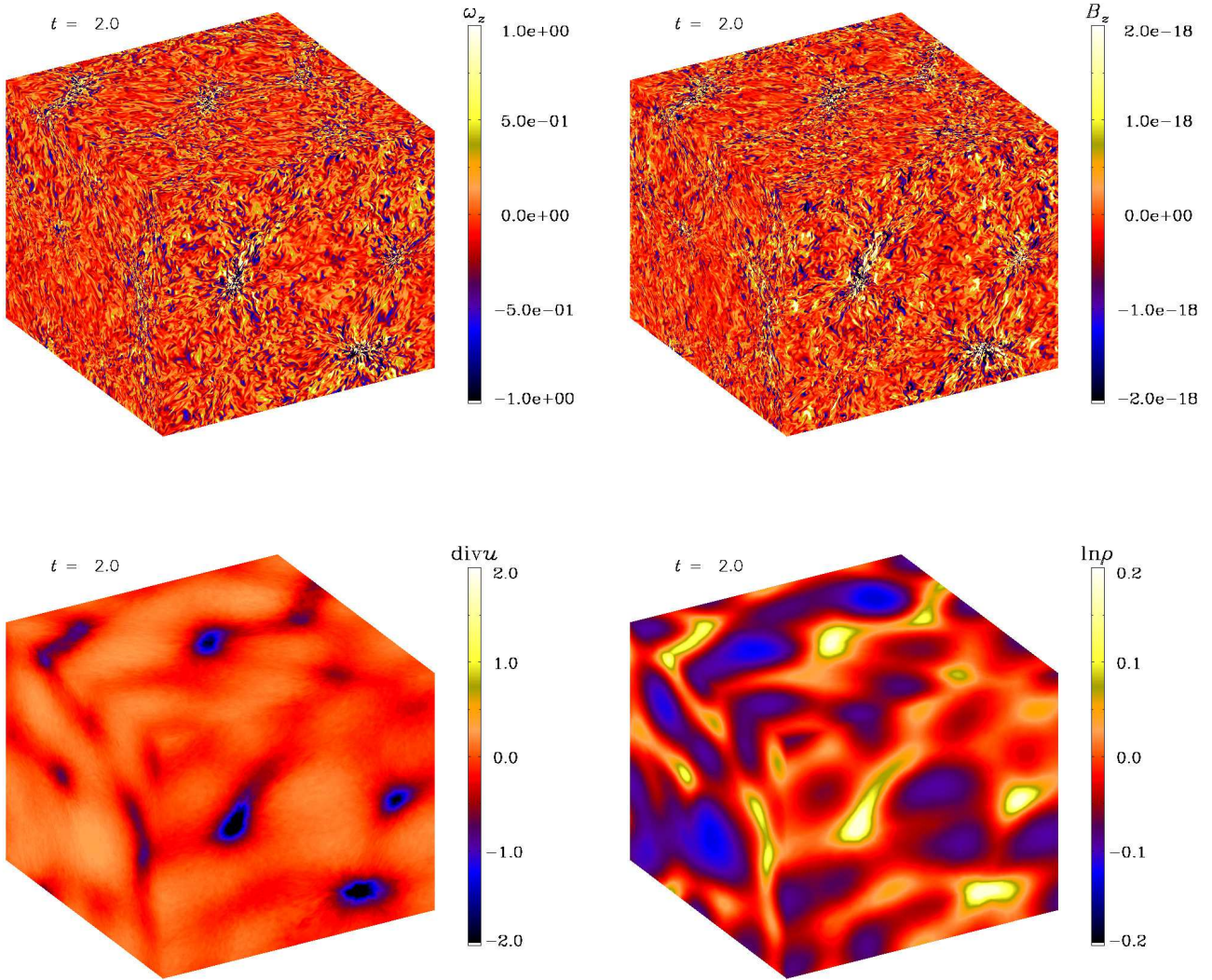


Figure 2. ω_z (upper left), B_z (upper right), $\nabla \cdot \mathbf{u}$ (lower left), and $\ln \rho$ (lower right) near the end of the run. Note the close correlation of the magnetic field with the vorticity and their concentration toward regions of strong flow convergence ($\text{div } \mathbf{u} < 0$) and high density.

our runs in Table 1. In Figure 2 we show a visualization of the z components of the vorticity and magnetic field for Run B, as well as its flow divergence and the logarithmic density near the end of the run at $tc_s k_1 = 2.02 = 5.24 t_{\text{ff}}$, shortly before further compression can no longer be resolved. The fact that this time is much longer than unity is due to the periodicity of the solution to the Poisson equation (Federrath & Klessen 2012; Lane et al. 2022). We see that ω_z and B_z show strong concentrations toward regions where the density also increases. Note that the regions of negative flow divergence are more strongly concentrated than those of positive flow divergence, but both $\nabla \cdot \mathbf{u}$ and $\ln \rho$ are dominated by a spatially smooth component that, unlike ω_z and B_z , lack small scales. Very weak small-scale perturbations can be seen in the visualizations of $\nabla \cdot \mathbf{u}$, but not in those of $\ln \rho$. Gradients of $\ln \rho$ do, however, show marked small-scale structure. In our runs, the density contours are more often aligned with

the magnetic field vector than being perpendicular to it. This is demonstrated in Appendix B for Runs M1 and I1, where we see that \mathbf{B} is mostly perpendicular to $\nabla \ln \rho$.

To see whether at any scale, the Reynolds number is large enough for dynamo action, we employ the k -dependent Reynolds numbers. In Figure 3, we show spectra of $\text{Re}(k)$ and $\text{Lu}(k)$ at different times. We clearly see that the spectra display instability for $k < k_J = 5 k_1$, and only at late times ($tc_s k_1 > 1.7$), somewhat smaller scales begin to grow as well. However, the effect on the rest of the spectrum is surprisingly weak. There is a small increase of $\text{Lu}(k)$ at all wavenumbers, but there is no visible effect from the Jeans instability itself, except for the time close to the end of the simulation where one sees an increase of both $\text{Re}(k)$ and $\text{Lu}(k)$ at the highest wavenumbers, indicating that more energy is now being channeled through the turbulent cascade. We also see that the value of $\text{Re}(k)$ near the wavenumber k_t , where the initial

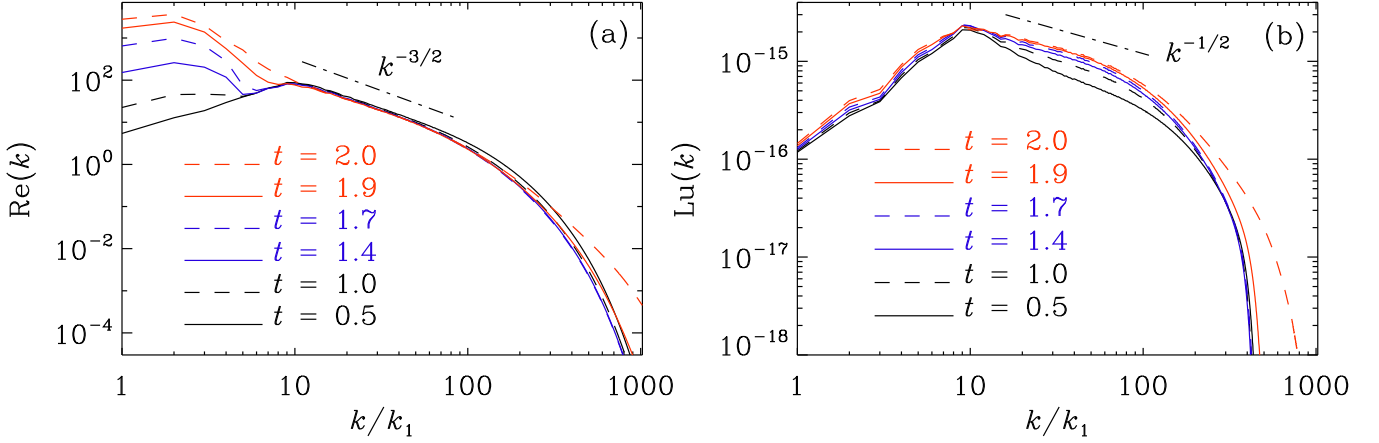


Figure 3. (a) $\text{Re}(k)$ and (b) $\text{Lu}(k)$ for Run B at six different times, indicated by line types and color.

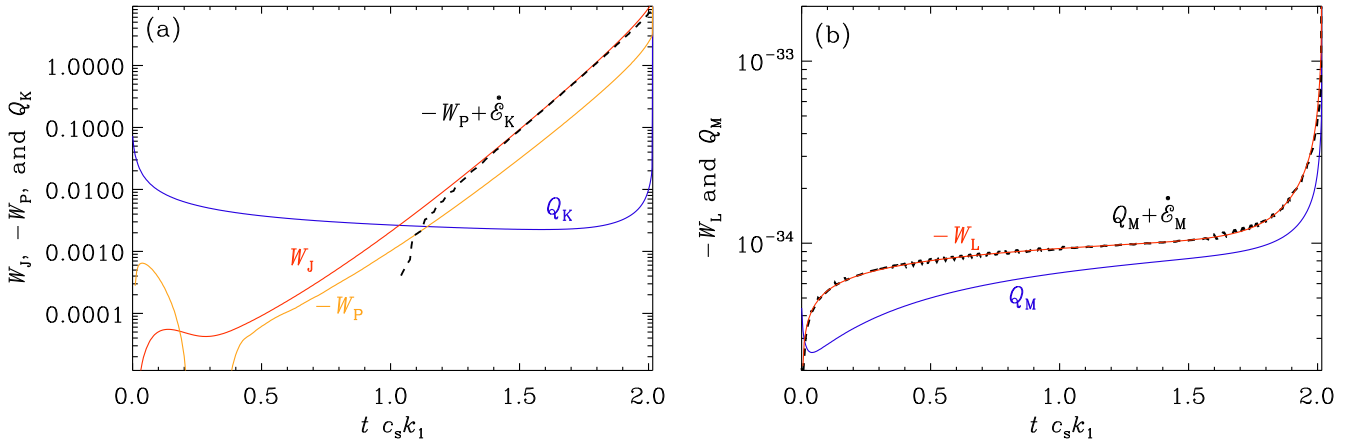


Figure 4. (a) Work terms W_J (red) and $-W_P$ (orange), as well as $-W_P + \dot{\mathcal{E}}_K$ (black dashed). Also shown is the kinetic energy dissipation, Q_K . (b) Work terms $-W_L$ (red) and Q_M (blue), as well as $Q_M + \dot{\mathcal{E}}_M$ (black dashed). We recall that all work terms are in units of $\rho_0 c_s^3 k_1$.

kinetic energy spectrum peaks, is around $\text{Re}_{k_f} = 100$. According to previous studies, this value is high enough for dynamo action. Our more detailed studies below confirm that this is indeed the case. When changing ν and η , the peak values of $\text{Re}(k)$ and $\text{Lu}(k)$ change correspondingly. In Appendix C, we show that $\text{Re}_{k_f} = 100$ is close (within a factor of two) to the Taylor microscale Reynolds number.

3.2 Work terms

Next, we consider the evolution of the various work terms; see Figure 4. The work done by the gravity force, $-\langle \rho \mathbf{u} \cdot \nabla \Phi \rangle \equiv W_J > 0$, leads to flow compression, $\langle p \nabla \cdot \mathbf{u} \rangle \equiv W_P < 0$, and an increase of the kinetic energy density, so

$$-\langle \rho \mathbf{u} \cdot \nabla \Phi \rangle = -\langle p \nabla \cdot \mathbf{u} \rangle + \frac{d\mathcal{E}_K}{dt} \dots, \quad (15)$$

where the ellipsis denotes the sum of two additional, subdominant terms: Q_K and $-W_L$. The dominant balance in the kinetic energy evolution is given by the Jeans work, which is found to be balanced to 1/3 by the pressure work and to 2/3

by the growth in kinetic energy, i.e.,

$$-W_P \approx \frac{1}{3} W_J, \quad \dot{\mathcal{E}}_K \approx \frac{2}{3} W_J. \quad (16)$$

The latter can be integrated to give $\mathcal{E}_K \approx (2/3) \int W_J dt$. Likewise, integrating Eq. (5) gives $-\mathcal{E}_P \approx \int W_J dt$, which implies $\alpha_{\text{vir}} = 2\mathcal{E}_K/|\mathcal{E}_P| \approx 4/3$. Its value would be unity, if only half of W_J went into the growth of kinetic energy, but this is not the case. It is important to realize that the energy flux ratios in Eq. (16) apply to the time $t = t_*$. They change at later times toward 1/4 and 3/4 for the pressure work and growth in kinetic energy; see Appendix A, which implies $\alpha_{\text{vir}} \approx 3/2$.

These ratios of the work terms implies that about one-third of the gravitational energy goes into compressional heating and two-thirds go into kinetic energy before eventually also being thermalized. At the reference time $t_* = 1.5/(c_s k_1)$, however, viscous dissipation contributes only about 3%; see Runs A–E in Table 1.

In the kinematic regime of the dynamo, the work done by the Lorentz force is very small; see Figure 4(b). Nevertheless, this term exceeds the Joule dissipation when Re is large enough. Here, the work done *against* the Lorentz force, $-W_L$, leads to Joule heating and an increase in the magnetic energy

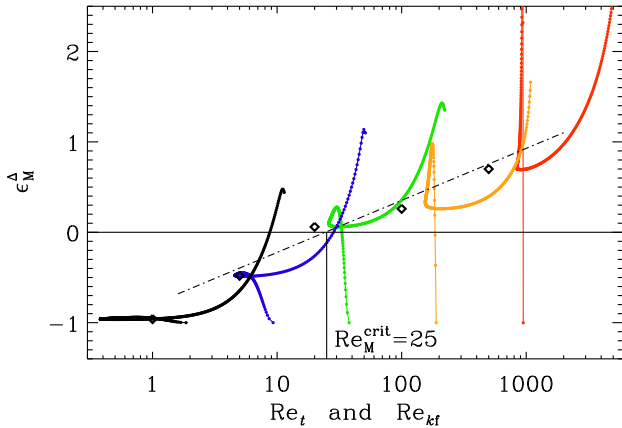


Figure 5. Time dependence of $(-W_L/Q_M) - 1$ on Re_t for Runs A (red), B (orange), C (green), D (blue), and E (black). The values of $(-W_L/Q_M) - 1$ from Table 1 are shown as diamonds as a function of Re_{k_f} and are seen to obey an approximate fit given by $\ln(0.45 \text{Re}^{1/4})$; see the dashed-dotted line.

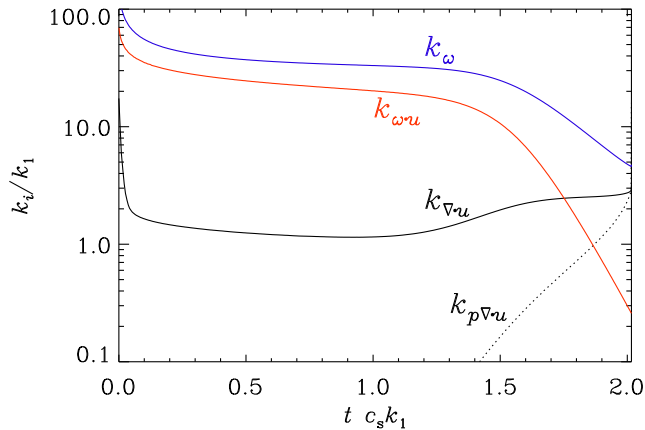


Figure 6. Characteristic wavenumbers k_ω (blue), $k_{\omega \cdot u}$ (red), $k_{\nabla \cdot u}$ (solid black), and $k_{p \nabla \cdot u}$ (dotted black).

density, i.e.,

$$-\langle \mathbf{u} \cdot (\mathbf{J} \times \mathbf{B}) \rangle = \langle \mu_0 \eta \mathbf{J}^2 \rangle + \frac{d\mathcal{E}_M}{dt}. \quad (17)$$

Therefore, based on the positivity of $(-W_L) - Q_M$, i.e., the positivity of γ , we argue that we can determine the threshold for dynamo action to be around 25. This is the value for which the interpolated line of $(-W_L/Q_M) - 1$ vs Re crosses zero, which corresponds to marginal dynamo excitation; Figure 5. In fact, Run C with $\text{Re}_{k_f} = 20$ is close to the marginal point; see Table 1.

During the exponential growth phase of the Jeans instability, the velocity grows at the rate $\sqrt{24}c_s k_1$. During that period, $\text{Re}(t)$ increases rapidly with time, and so does also the difference $(-W_L) - Q_M$.

3.3 Dependence on the magnetic Reynolds number

As the magnetic Reynolds number increases, we expect a dynamo to become stronger and thus, $\epsilon_M^\Delta \equiv (-W_L - Q_M)/Q_M$

to increase. However, the magnetic Reynolds number is time-dependent, because u_{rms} increases. This raises the question whether this dependence follows a similar trend that is seen by comparing different runs.

In Figure 5 we plot $\epsilon_M^\Delta(t)$ versus Re_t and compare with the values listed in Table 1 for the nominal time $t_* = 1.5/(c_s k_1)$ versus Re_{k_f} . We see that $\epsilon_M^\Delta(t_*)$ shows a rather shallow increase with $\text{Re}_M(t_*)$ of the form

$$\epsilon_M^\Delta \approx \ln(0.45 \text{Re}^{1/4}). \quad (18)$$

The time-dependent tracks do approximately match this dependence at around intermediate times, but all the lines are curved and shallower for early times and steeper at late times, where the Jeans instability becomes dominant.

3.4 Compression and vorticity

The magnetic field growth seems to be strongly correlated with the rms vorticity. Earlier studies showed that it is only the vortical part of the flow that leads to dynamo action (Mee & Brandenburg 2006). To quantify the relative importance of vortical and irrotational or compressive contributions to the velocity field, we show in Figure 6 the evolution of the characteristic wavenumbers k_ω , $k_{\omega \cdot u}$, $k_{\nabla \cdot u}$, and $k_{p \nabla \cdot u}$.

We see that $k_\omega \approx 35$ and $k_{\omega \cdot u} \approx 20$ during the early phase when the collapse velocity is still subdominant. When the collapse becomes dominant, k_ω and $k_{\omega \cdot u}$ rapidly decline and $k_{\nabla \cdot u} \approx 2.5$ prior to the final collapse. Nevertheless, we always find $k_\omega > k_{\nabla \cdot u}$, i.e., vorticity is still important. This is partially because of the compression of vortices, as seen in Figure 2, which enhances the vorticity. Furthermore, we find that $k_{p \nabla \cdot u} \ll k_{\nabla \cdot u}$, except very close to the collapse when the two are similar.

3.5 Dependence on resolution

For our reference models, we use a fairly high resolution of 2048^3 mesh points. Larger resolutions become easily impracticable and reach computational memory limitations. However, the dependence on resolution is small and the maximum run time before the collapse stops the calculation hardly changes at all when increasing the resolution by a factor of two. By comparing Runs b and B, we see that the values of W_P/W_J and $\dot{\mathcal{E}}_K/W_J$, as well as those of $\dot{\mathcal{E}}_M/(-W_L)$ and $Q_M/(-W_L)$ agree with each other within 10%.

4 RESULTS FOR STRONG MAGNETIC FIELDS

4.1 Earlier collapse with stronger fields

We now consider cases where the magnetic field is dynamically important. This situation is of particular interest for dense pre-stellar cores, where the measured (e.g., Crutcher 2012) or inferred (e.g., Karoly et al. 2020; Pattle et al. 2021) magnetic fields are particularly strong.

Figure 7 shows a comparison of the magnetic field patterns for Runs M3 and M1, i.e., for weaker and stronger fields, respectively. For the stronger magnetic fields in Run M1, the magnetic eddies appear to be organized in larger patches that correspond to over- or underdense regions. For the stronger magnetic fields in Run M1, the magnetic eddies appear earlier

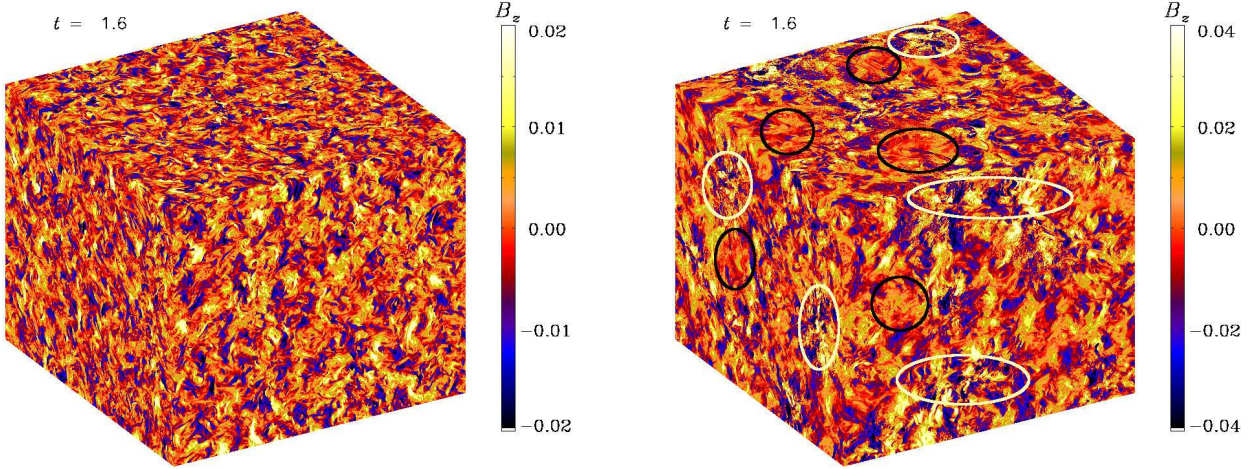


Figure 7. B_z for Runs M2 (left) and M1 (right) at $t c_s k_1 = 1.6$. Note the large-scale concentrations (marked by white ellipses) and voids (marked by black circles) for stronger fields, even though the stage of the collapse is the same. For Run M1, one sees indications that the 2048^3 resolution begins to become insufficient at $t = 1.6$.

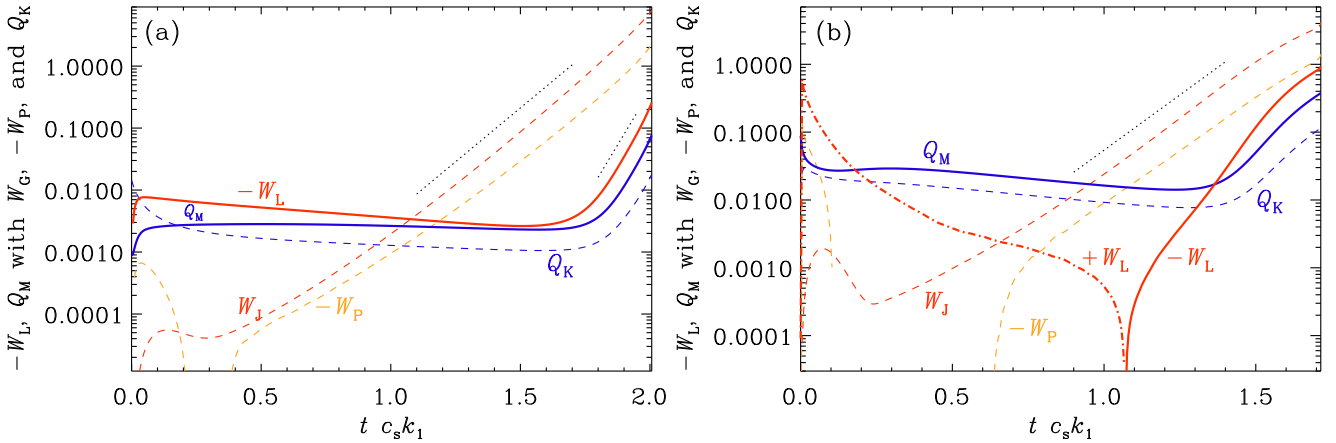


Figure 8. Work terms $-W_L$ (solid red) and Q_M (solid blue), together with W_J (dashed red) and $-W_P$ (dashed orange), as well as Q_K (dashed blue) for (a) Run M3 with a relatively weak magnetic field and (b) Run M1 with a strong magnetic field. Dotted lines denote the slopes corresponding to the growth rates $1.6\sigma_J$ and $3.2\sigma_J$ in panel (a) and $1.5\sigma_J$ in panel (b). The thick dashed-dotted line in panel (b) denotes $W_L > 0$. Note that the work terms are in units of $\rho_0 c_s^3 k_1$.

than in Run M3, which is probably the result of the magnetically driven motion early on; see Figure 1. This behavior is suggestive of an accelerated collapse process. This is an important difference to the standard paradigm of magnetically controlled star formation that employs a uniform magnetic field (Mestel & Spitzer 1956; Mouschovias & Spitzer 1976; Shu 1977). Instead, here the magnetic field is turbulent and only has moderate large-scale coherence.

4.2 When W_L affects the collapse

In Figures 8(a) and (b) we show the work terms for Runs M3 and M1, respectively. Again, we see that a turbulent magnetic

field does not systematically delay the collapse, and a strong field can even accelerate it.

We also see that the late-time exponential increase of $-W_L$ and Q_M changes with respect to the weak-field behavior from being twice the rate of W_J to being equal to it; see Figure 8(b). Assuming the change in $\mathbf{J} \times \mathbf{B}$ to be itself proportional to the change in \mathbf{u} , we see that $-W_L$ is quadratic in \mathbf{u} , which explains the growth of $-W_L$ at twice to Jeans rate. Once the field is strong, $\mathbf{J} \times \mathbf{B}$ does not change much anymore, and so $-W_L$ only grows at the Jeans rate.

The gravitational collapse is primarily characterized by the increase in the velocity \mathbf{u} and not so much by a change in gravity. In reality, however, the change in gravity does con-

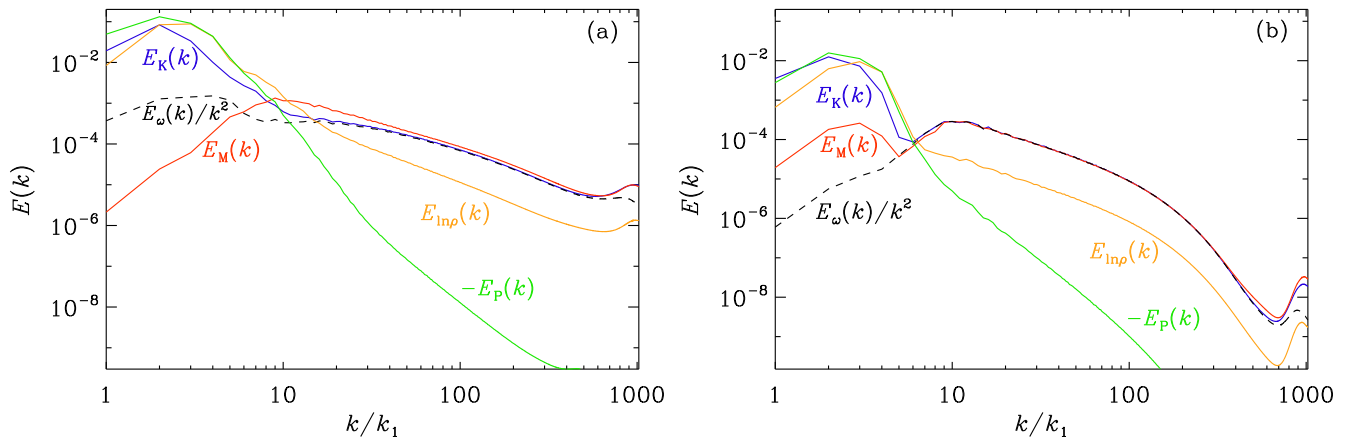


Figure 9. Comparison of kinetic, magnetic, and potential energy and density spectra at $tc_s k_1 = 1.7$ for (a) Run M1 with a strong turbulent initial magnetic field and (b) Run I1 with a strong uniform initial magnetic field. The dashed lines denoted with $E_\omega(k)/k^2$ correspond to kinetic energy spectra of the vortical part of the velocity. Here, the $E(k)$ are in units of $c_s^2 k_1^{-1}$. Note that both axis ranges in (a) and (b) are the same.

tribute about 50%, and so we find that W_J increases at a rate of about $1.6 \sigma_J$, and $-W_L$ increases at a rate of about $3.2 \sigma_J$.

4.3 Comparison with uniform initial magnetic fields

In Figure 9(a) we show kinetic and magnetic energy spectra together with logarithmic density spectra and the normalized enstrophy spectra representing the kinetic energy spectra of the vortical part, and compare with the case of a uniform initial magnetic field in Figure 9(b). The two panels correspond to Runs M1 and I1. Even though Lu_{t_*} is 25% higher in I1, the spectral energies are lower. The density spectra show a rapid increase for $k \leq k_J$, which is associated with the Jeans instability, as was already seen in the kinetic energy spectra; see Figure 3(a).

The magnetic energy spectra and the kinetic energy spectra of the vortical part do not show the same increase, but there is a slight one, which is different for the cases with a turbulent and an initially uniform field. To understand this, it is useful to discuss now the kinetic and magnetic helicity spectra for the two cases. We see that, for runs with an initially uniform magnetic field at intermediate wavenumbers, the magnetic energy is either in nearly perfect equipartition, or in super-equipartition with the kinetic energy. However, it becomes subdominant at small wavenumbers, where the behavior is affected by gravitational collapse. Therefore, the spectrum resembles that of a small-scale dynamo, where the magnetic field is also in super-equipartition at large k ; see Haugen et al. (2003, 2004a). However, this similarity should not be regarded in any way as evidence in favor of a dynamo. It appears to be instead just a typical behavior of any type of hydromagnetic turbulence.

Returning to the slight uprise of the magnetic field for $1 \leq k/k_1 < 5$ in the case of an initially uniform magnetic field, we argue that this is caused by the tangling of the magnetic field by the collapsing gas motions. It is therefore not due to an inverse cascade, which usually occurs only in the absence of a mean magnetic flux through the domain. In the case of a turbulent magnetic field, the build-up of vorticity at small wavenumbers could be caused by the shear flows, which

leads to what is known as a vorticity dynamo (Elperin et al. 2003). In the case of an initially uniform magnetic field, this vorticity dynamo is suppressed (Käpylä et al. 2009). However, the uprise of the vortical part of the velocity field for $1 \leq k/k_1 < 5$ appears to be caused by the magnetic field and becomes weaker for Runs M2 and M3.

4.4 Helicity spectra

It is important to realize that, owing to the use of periodic boundary conditions, an initially uniform magnetic field is equivalent to what is sometimes described as an imposed magnetic field. This is simply because the mean magnetic flux is preserved. A well-known difference between cases with and without an imposed magnetic field is the fact that $\langle \mathbf{A} \cdot \mathbf{B} \rangle$ is no longer conserved in the former case (Berger 1997). This is because now the magnetic helicity in the domain interacts with the magnetic helicity on scales larger than the size of the periodic domain, but this part is no longer included in the simulation; see the discussion in Brandenburg & Matthaeus (2004). In simulations of decaying turbulence, it has been found that the magnetic fluctuations decay more rapidly when there is an imposed magnetic field (Brandenburg et al. 2020).

Figure 10 shows kinetic and magnetic helicity spectra for the cases with a turbulent and an imposed field for runs with different magnetic field strengths. The kinetic helicity spectra are similar in the two cases, but the magnetic helicity spectra are not. In the case of an imposed magnetic field, there is magnetic helicity of the same sign at all wavenumbers, although it is less strong at small wavenumbers. By contrast, in the case with a turbulent magnetic field with zero net flux, the magnetic helicity is predominantly of opposite (negative) sign and relatively strong also at small wavenumbers, except in the case with the strongest magnetic field (Run M1). This is caused by magnetic helicity conservation, where a small-scale driving of magnetic helicity of one sign causes automatically the appearance of magnetic helicity of opposite sign at large scales; see also Brandenburg et al. (2019) for similar results. The small-scale magnetic helicity does get slowly dissipated at late times through finite microphysical magnetic diffusiv-

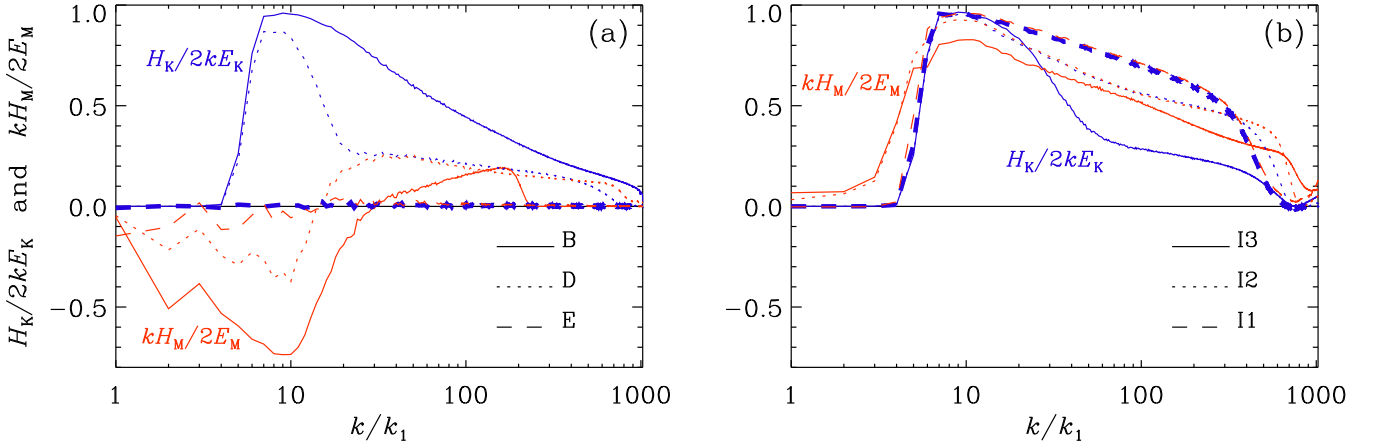


Figure 10. Comparison of relative helicity spectra with (a) turbulent and (b) uniform initial magnetic fields. Blue (red) lines denote kinetic (magnetic) relative helicity spectra. The solid lines are for Run B (I3), the dotted lines are for Run D (I2), and the thick dashed lines are for Run E (I1) for turbulent (uniform) initial magnetic fields.

ity, leaving predominantly the large-scale magnetic helicity of opposite sign behind.

4.5 Contributions to the Lorentz work

The work done against the Lorentz force serves as one of our main tools to quantify dynamo action. As we have mentioned at the end of Sect. 2.2.1, the work done against the Lorentz force can be subdivided into contributions from the magnetic pressure gradient, the tension force, and the curvature force. In Figure 11, we show that, for weak initial magnetic fields, the most important contribution to the pseudo growth rate comes from the work done against the curvature force, but later during the collapse, a more important contribution comes from the compressional work done against the magnetic pressure gradient.

In the runs with a strong magnetic field (turbulent or imposed), the value of γ is still negative at the critical time t_* , but the compressional work done against the magnetic pressure gradient is positive, and it was positive also during the earlier phase, especially in the case of a turbulent magnetic field; see Figure 11(c). The contribution of γ_c is a characteristic feature of amplification or at least sustenance of the magnetic field in collapsing turbulence through compression.

In Figure 12 we plot the time dependences of γ , γ_{2D} , and $\gamma_{3D} = \gamma - \gamma_{2D}$. We see that γ_{2D} is always close to zero, except during an early phase which can be associated with 2-D tangling of the initial magnetic field. When γ_{3D} is included, the resulting pseudo growth rate is positive during much of the early part of the evolution.

Based on the positive values of γ_{\perp} and γ_{3D} in the cases of weak magnetic fields in Figures 11 and 12, we are led to suggest that those runs do indeed host supercritical dynamos. When the magnetic field is strong, however, γ_{\perp} and γ_{3D} are now negative, suggesting that Run M1 cannot be classified as a dynamo.

For strong magnetic fields, only near the end of the collapse does γ_{\perp} become positive. On the other hand, γ_{3D} becomes then the dominant term during the collapse and γ_{2D} becomes negative; see Figure 12(b). This is probably caused

by the strong alteration of the flow by the magnetic field, making now γ_{2D} strongly negative. This increases the compression and tangling terms associated with γ_{2D} , which then contribute to enhancing the kinetic energy rather than the other way around (as in a dynamo). Nevertheless, since the magnetic field is now increasing, γ_{3D} becomes positive. From Figures 11(c) and (d) we know, however, that this increase is manifestly caused by compression, which must therefore be a 3-D compression, and not a dynamo effect.

In summary, we are led to conclude that there is dynamo action in all cases with weak magnetic fields prior to collapse, but probably no longer or not very much during the actual collapse. When the magnetic field is already strong, there is no longer dynamo action, but just 3-D compression. For large Mach numbers, at late stages of the collapse, shocks form and cross each other, which causes vorticity production (Porter et al. 2015), resulting then also in dynamo action (Federrath et al. 2011a). However, this happens at such small scales and such late times that this effect cannot be captured in direct numerical simulations, even at a resolution of 2048^3 mesh points. After $t_{cs}k_1 = 1.98$, the Jeans length is no longer resolved with 30 grid cells – the minimum proposed by Federrath et al. (2011b); see Appendix D, where we show the evolution of the maximum density during the collapse.

4.6 Waves in the density spectra

Before concluding, let us comment on an interesting feature that we noticed in spectra of the logarithmic density. At early and intermediate times, we see a wavy structure in $E_{\ln \rho}(k)$; see Figure 13. In fact, this wavy modulation is of the form $\cos k\xi(t)$, where $\xi(t) = c_s t$ is the distance a sound wave has propagated in the time t since the initial condition was applied. As time goes on, and as $\xi(t)$ therefore increases, the waves appear to propagate toward smaller values of k and are of progressively shorter length in k space. The changing phase of these waves can be described by the formula

$$E_{\ln \rho}(k, t) = E_{\rho}^{(0)}(k) [1 + g(k, t) (1 - \cos kc_s t)], \quad (19)$$

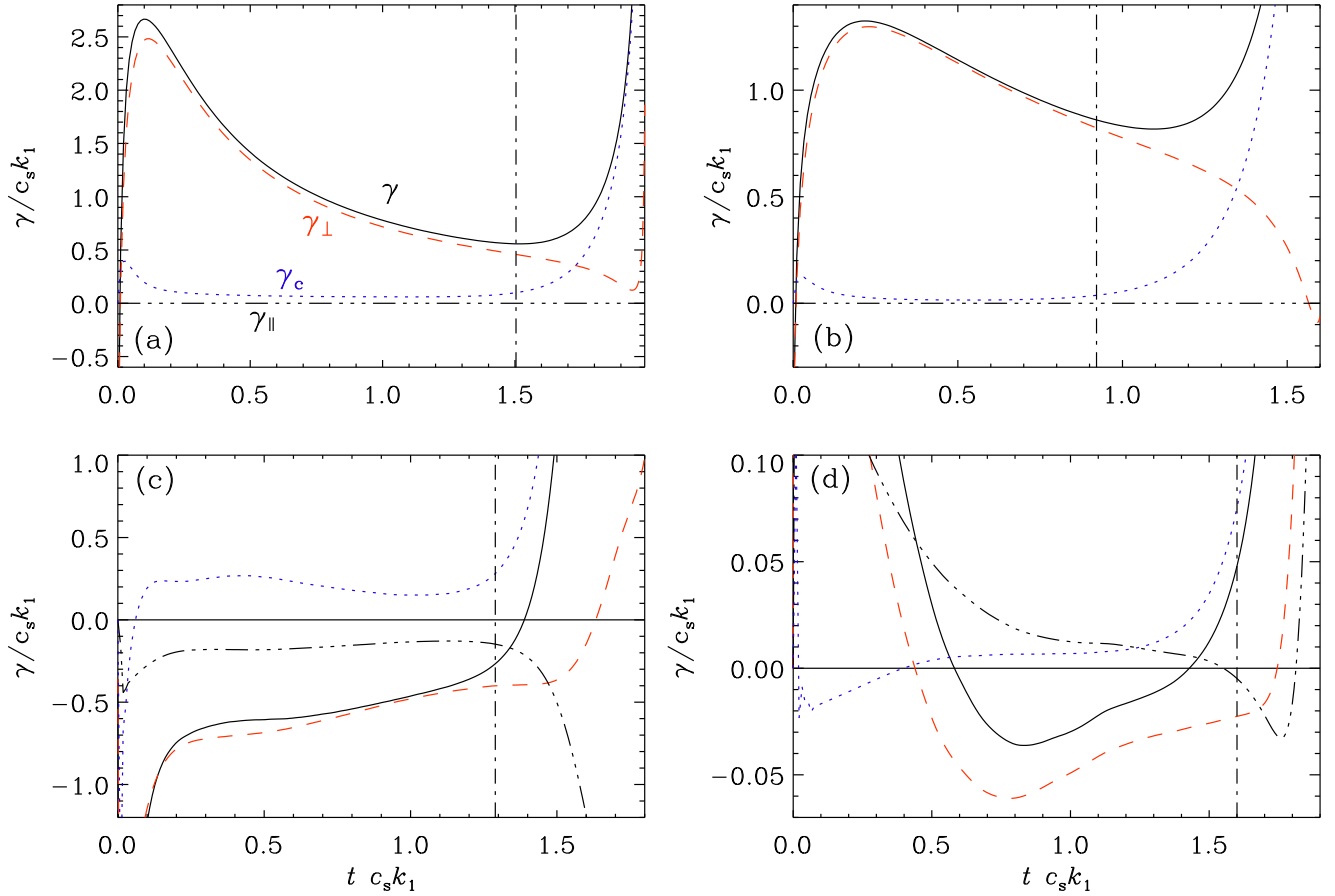


Figure 11. Evolution of the pseudo growth rate $\gamma = \gamma_c + \gamma_{\parallel} + \gamma_{\perp}$ (solid lines), with contributions from the work done against the curvature force (γ_{\perp} , red dashed lines), the tension force (γ_{\parallel} , black dashed-triple-dotted lines), and the magnetic pressure gradient (γ_c , blue dotted lines) for (a) Run B, (b) Run O2, (c) Run M1, and (d) Run I1. In panels (a) and (b), $\gamma_{\parallel} = 0$. In panels (c) and (d), $\gamma_{\parallel} \neq 0$, and the zero line has been drawn as a straight black line. The vertical dashed-dotted lines denote the critical time t_* when the Mach number has recovered to the original value of about 0.2.

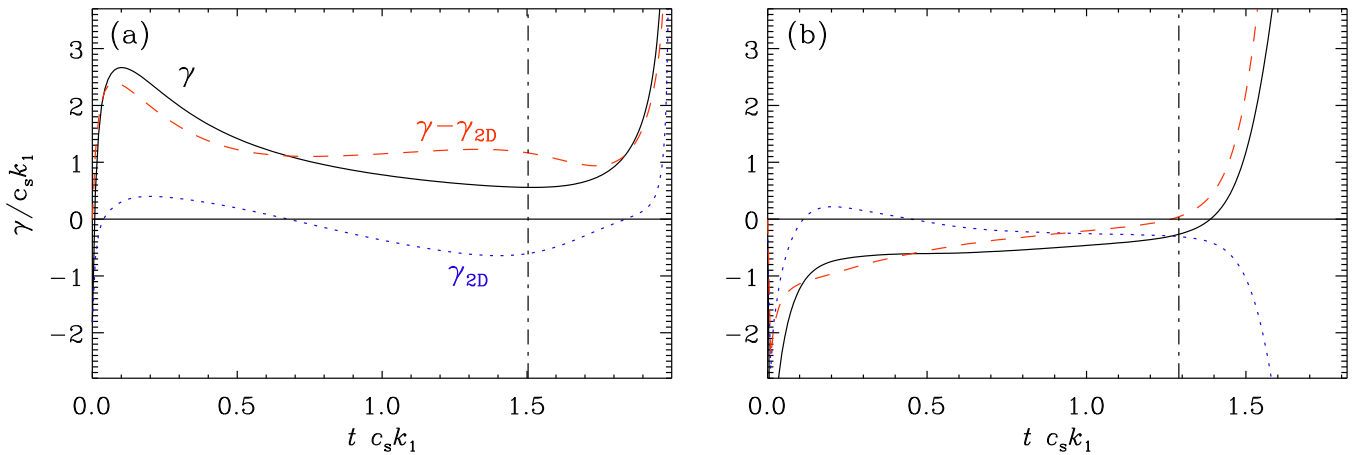


Figure 12. Evolution of the pseudo growth rate γ (black lines), with contributions from γ_{2D} (blue lines) and the residual $\gamma - \gamma_{2D}$ (red lines), for (a) Run B and (b) Run M1.

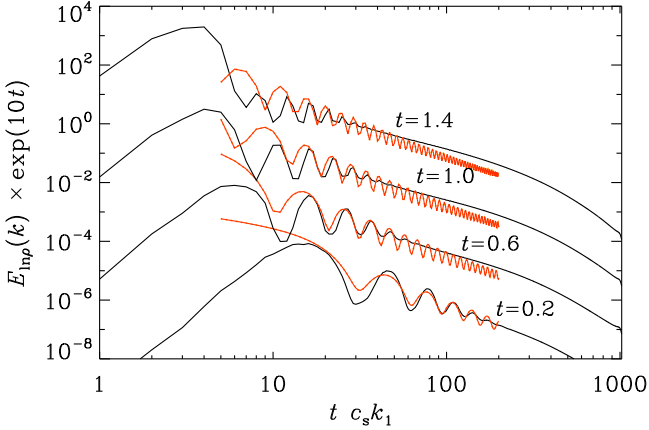


Figure 13. Density spectra at $t = 0.2, 0.6, 1,$ and 1.4 , shifted upward by an $\exp(10t)$ factor to be able to see the shift of the oscillations in the spectra in k . The dotted orange lines denote approximate fits of the form given by Eq. (19).

where $E_{\rho}^{(0)}(k) \propto k^{-5/3}$ denotes the unmodulated spectrum, and $g(t) = (140/k) \exp(-0.8t)$ is an empirically defined function (in code units). Only at later times, the fit is going somewhat out of phase. Given the agreement of our hypothetical modulation of the form $\cos k\xi(t)$ with the actual spectrum, we can argue that the wavy structure is indeed caused by the initial velocity perturbation launching sound waves from multiple locations in the domain all at the same time, and that their characteristic scale increases with time like $\xi(t) = c_s t$. Similar waves have also been seen in simulations of gravitational waves that are being initiated from an instantaneous perturbation; see Figure 2 of Roper Pol et al. (2020). No explanation for this phenomenon was offered there, but we have now confirmed that it can be explained in a similar way, except that the relevant speed in the expression for $\xi(t)$ is the speed of light.

5 CONCLUSIONS

In the present work, we have used the instantaneous excess of the work done by the Lorentz force over the Joule dissipation as a quantity that characterizes the dynamo. Under stationary conditions, the dynamo can easily be characterized by the growth rate. However, a growth rate cannot be defined in situations when the velocity itself decays or grows exponentially with time, like we observe in our models.

The dynamo criterion based on the work terms results in a value of the critical Reynolds number of about 25, which is smaller than the critical value of about 35 for small-scale dynamo action (Haugen et al. 2004a), but larger than the value for large-scale dynamo action in the presence of helicity of below six (Brandenburg 2009). Also, in the present case there is helicity, so we do expect a critical value that is less than 35. However, there is a strong contribution from irrotational motions that makes the dynamo harder to excite and does itself not contribute to dynamo action (Mee & Brandenburg 2006). During the collapse, i.e., after $t = t_*$, and for weak magnetic fields (Runs B and O2), γ_{\perp} and γ_{3D} show a slight decrease when the magnetic field is weak, supporting the idea

that this magnetic field growth is not primarily caused by dynamo action, but just by compression.

Our investigation shows that the most important contribution to the growth of a magnetic field comes from the work done against the curvature force, although later during the collapse, there is an even more important contribution from the compressional work done against the magnetic pressure gradient. However, as we have argued above, this type of magnetic field amplification happens also in one or two dimensions and should therefore not be associated with dynamo action. By considering the decomposition into γ_{2D} and γ_{3D} we have made an attempt of distinguishing dynamo action from the type of non-dynamo amplification seen also in two dimensions. Nevertheless, our dynamo criterion is not very precise, as the pseudo growth rate changes behavior with different initial conditions and a number of factors need to be considered in combination.

We stated in the introduction that the exact fraction of potential energy that goes into turbulence is unknown. Our results now show that one-third of the energy input from potential energy goes into compressional heating, and two-third goes into the kinetic and magnetic energies of the turbulence. Thus, one would expect that, at the end of the collapse, the sum of kinetic and magnetic energy densities is twice the thermal energy density from compressive heating. This is different from the virial theorem, which relates potential and kinetic energies to each other. As explained in Sect. 3.2, however, since the two-third contribution to the kinetic energy comes from potential energy, which becomes more negative with time, it follows that the ratio of kinetic to potential energy is $2/3$ and thus, the virial parameter is $4/3$. It would be unity, if the contribution to the kinetic energy was half the Jeans work. At later times, however, the fractional kinetic energy gain increases toward $3/4$ of the Jeans work, which implies a virial parameter of about $3/2$.

In all the simulations presented here, we have used an isothermal equation of state. However, deviations from isothermality probably play an important role during molecular cloud collapse. For example, Lee & Hennebelle (2018) caution that, in simulations studying gravitational fragmentation of molecular clouds, an isothermal equation of state cannot lead to converged results with increasing numerical resolution. They propose that an adiabatic equation of state at high densities, essentially accounting for the formation of the Larson core is a more physically meaningful approach. In future work, it would be interesting to perform simulations using an ideal gas equation of state instead of an isothermal one. Such simulations could also allow for cooling, which would further increase the density in regions of strong flow convergence and counteract an otherwise singular collapse.

It would also be interesting to apply our analyses to earlier work that uses Bonnor-Ebert spheres as initial conditions (Sur et al. 2010, 2012; Federrath et al. 2011b). Bonnor-Ebert spheres are nonuniform equilibria in a non-expanding finite space, so there is no ρ_0 term in Eq. (1). Our simulations never go through such a state or reach any near-equilibrium state. Starting with a Bonnor-Ebert sphere could lead to the collapse proceeding in a different way from ours. If the collapse occurs sufficiently slowly, it could be easier to achieve dynamo growth rates that remain faster than the collapse rate for a longer time.

Another useful extension would be to compare with simu-

lations that make use of adaptive mesh refinement (see, for example, Federrath et al. 2010). Such simulations would have varying accuracy in space, and it is currently unclear how this affects the kinetic and magnetic energy spectra and other diagnostics. Since the varying accuracy is not a concern in the present simulations, they can be used as a benchmark. Another advantage of the present simulations is the fact that the viscosity and magnetic diffusivity are fixed and that therefore numerically converged and accurate results are possible.

ACKNOWLEDGEMENTS

We thank the referee for useful comments and references. This work was supported in part through the Swedish Research Council, grant 2019-04234. EN acknowledges funding by the ERC Grant ‘‘Interstellar’’ (Grant agreement 740120) and the Hellenic Foundation for Research and Innovation (Project number 224). Nordita is supported in part by Nordforsk. We acknowledge the allocation of computing resources provided by the Swedish National Infrastructure for Computing (SNIC) at the PDC Center for High Performance Computing Stockholm and the National Supercomputer Centre (NSC) at Linköping.

Code and data availability. The source code used for the simulations of this study, the PENCIL CODE (Pencil Code Collaboration et al. 2021), is freely available on <https://github.com/pencil-code/>. The DOI of the code is <https://doi.org/10.5281/zenodo.2315093>. The simulation setup and the corresponding data are freely available on <https://doi.org/10.5281/zenodo.5760126>; see also <https://www.nordita.org/~brandenb/projects/SelfGrav> for easier access to the same material as on the Zenodo site.

APPENDIX A: VIRIAL PARAMETER

In Sect. 2.2.1, we noted that $\alpha_{\text{vir}} = 2\mathcal{E}_K/|\mathcal{E}_P|$ is expected to be around unity, but that its value can be different at large Mach numbers and for strong magnetic fields. We have also stated that a value of $4/3$ is expected if $2/3$ of the Jeans work goes into building up kinetic energy. The purpose of this appendix is now to compare the evolution of α_{vir} for runs with strong magnetic field (Run M1), larger Mach number (Run S), with a subsonic run with weak magnetic field (Run B).

Initially, when the density is uniform, the potential energy density $\mathcal{E}_P = -\langle(\nabla\Phi)^2\rangle/8\pi G$ is small,¹ so α_{vir} is large. However, when the collapse has started, deep potential wells develop and $|\mathcal{E}_P|$ increases with $\mathcal{E}_P < 0$, so α_{vir} drops and eventually settles at a value of around 1.5 for weak magnetic fields (Run B), and perhaps also for the supersonic run before the collapse occurred (Run S); see Figure A1(a). This larger value $\alpha_{\text{vir}} \approx 1.5$ is caused primarily by the fact that the fractional kinetic energy gain from the Jeans work in Eq. (16) increases with time from $2/3$ to $3/4$; see Figure A1(b). At the

¹ Using the identity $\nabla \cdot (\Phi \nabla \Phi) = (\nabla \Phi)^2 + \Phi \nabla^2 \Phi$, the potential energy density can also be written as $\mathcal{E}_P = -\langle \rho \Phi \rangle / 2$, where we have made use of periodicity and the fact that $\langle \Phi \rangle = 0$. This yields $\dot{\mathcal{E}}_P = -\langle \nabla \Phi \cdot \nabla \Phi \rangle / 4\pi G = -\langle \rho \Phi \rangle$, which leads to Eq. (5) after using Eq. (3).

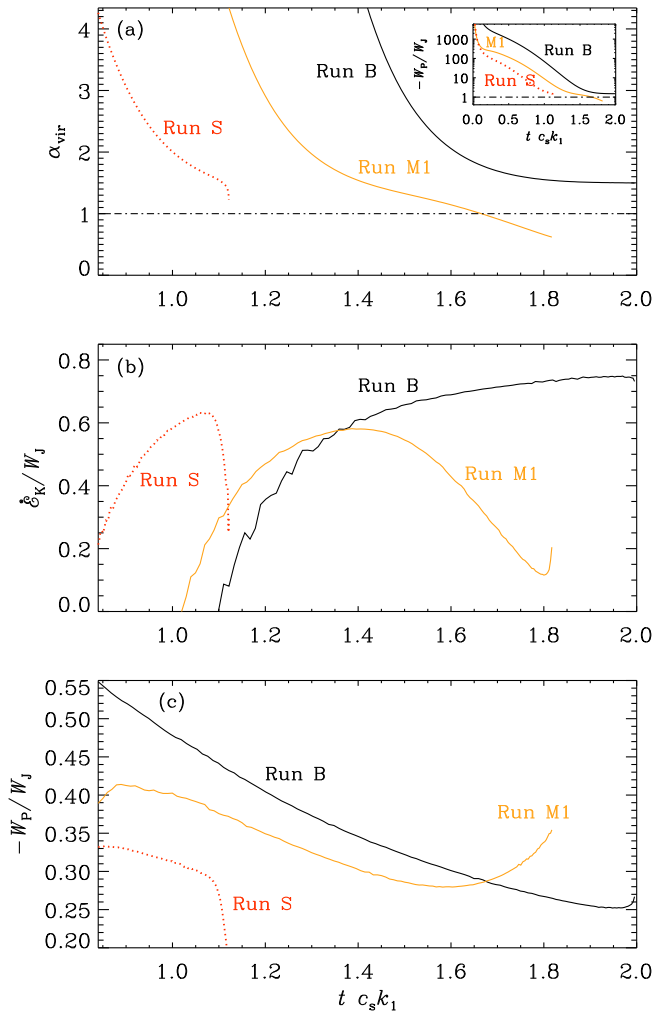


Figure A1. Time evolution of (a) the virial parameter, (b) the fractional kinetic energy gain, and (c) the fractional pressure work for Runs B, M1, and S. In (a), the inset is a logarithmic representation of α_{vir} over a larger range. At the end of Runs S and M1, the results are affected by insufficient resolution and cannot be trusted.

same time, the fractional pressure work decreases correspondingly from $1/3$ to $1/4$; see Figure A1(c). For strong magnetic fields (Run M1), α_{vir} continues to decrease below unity; see Figure A1.

APPENDIX B: GROWTH OF AND RELATION BETWEEN MAGNETIC FIELD AND DENSITY

The purpose of this appendix is to assess the role of the density in determining a relevant measure of the magnetic field in collapsing turbulence. During radial collapse, a uniform magnetic field is amplified such that the ratio $|\mathbf{B}|/\rho^{2/3}$ is constant (Pudritz et al. 2006). Therefore, it is customary to monitor the evolution of this quantity (Sur et al. 2010, 2012; Federrath et al. 2011b; Sharda et al. 2021). As a suitable volume average, one can consider $|\mathbf{B}|/\rho^{2/3} \sim \langle \mathbf{B}^2 / \rho^{4/3} \rangle^{1/2}$. In Figure B1, we show that for Runs B and M1, the quantities $\langle \mathbf{B}^2 / \rho^{2n} \rangle^{1/2} / \rho_0^n$ are nearly the same for

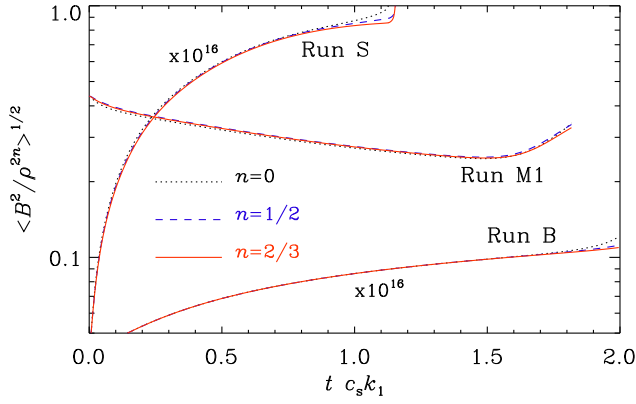


Figure B1. Different scalings of the magnetic field strength as a function of time (scaled up by 10^{16} for Runs B and S). Note that the units of $\langle B^2 / \rho^{2n} \rangle^{1/2}$ are $c_s \mu_0^{1/2} \rho_0^{1/2-n}$.

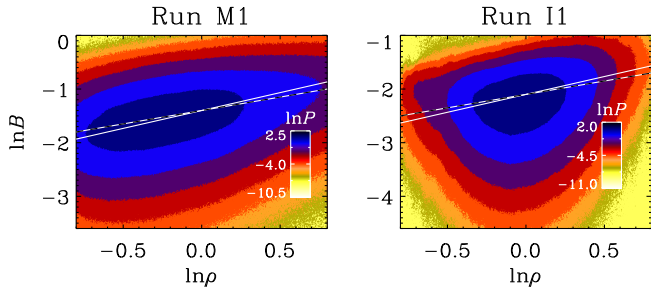


Figure B2. Logarithm of 2-D histograms $P(\ln \rho, \ln |\mathbf{B}|)$ for Runs M1 and I1. The solid and dashed lines correspond to $|\mathbf{B}| \sim \rho^{2/3}$ and $|\mathbf{B}| \sim \rho^{1/2}$, respectively.

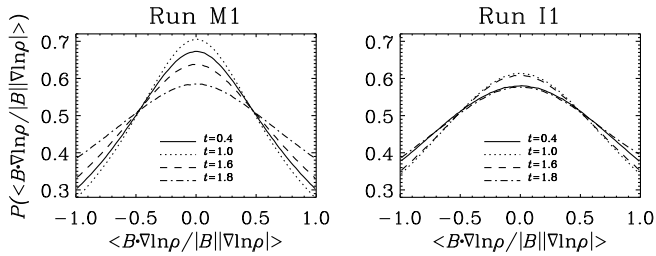


Figure B3. Histograms $P(\mathbf{B} \cdot \nabla \ln \rho / |\mathbf{B}| / |\nabla \ln \rho|)$ for Runs M1 and I1, for different times.

different exponents n . For Run S, the differences for different n are somewhat larger, but the differences between the cases $n = 1/2$ and $n = 2/3$ are still negligible. This justifies the use of v_A^{rms} in Figure 1 of the main text, which corresponds to $n = 1/2$ in Figure B1. In fact, also the case $n = 1/2$ has been discussed previously in the context of gravitational collapse (Crutcher 1999). In Figure B2, we present the logarithm of 2-D histograms $P(\ln \rho, \ln |\mathbf{B}|)$ to show that most of the points in the volume lie within elliptical islands stretched along the line $|\mathbf{B}| \sim \rho^{2/3}$. They are normalized such that $\int P(\ln \rho, \ln |\mathbf{B}|) d \ln \rho d \ln |\mathbf{B}| = 1$. This behavior has been observed in numerous simulations of self-gravitating turbulence (e.g. Soler et al. 2013; Chen et al.

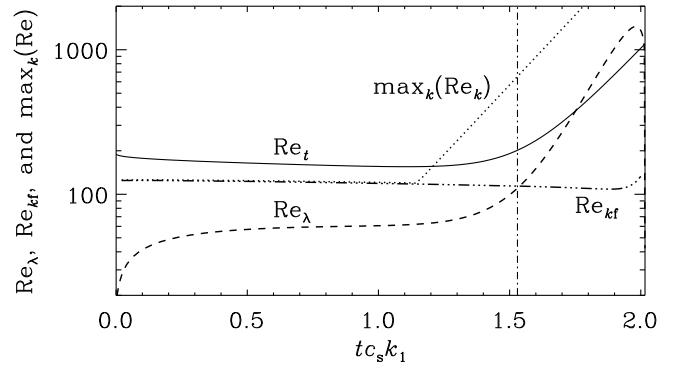


Figure C1. Comparison of the evolution of the Taylor microscale Reynolds number with other Reynolds numbers for Run B.

2016; Barreto-Mota et al. 2021), as a result of the converging motions driven by gravity (Soler & Hennebelle 2017).

In Sect. 3.1, we mentioned that $\ln \rho$ lacks small-scale structure, and that only $\nabla \ln \rho$ displays noticeable small-scale variations. In Figure B3 we present histograms of the cosine of the angle between \mathbf{B} and the logarithmic density gradients, $P(\mathbf{B} \cdot \nabla \ln \rho / |\mathbf{B}| |\nabla \ln \rho|)$, for Runs M1 and I1 at different times. They show that \mathbf{B} is mostly perpendicular to $\nabla \ln \rho$, i.e., the magnetic field lines tend to be aligned with the contours of $\ln \rho$.

APPENDIX C: COMPARISON WITH THE TAYLOR MICROSCALE REYNOLDS NUMBER

In Figure C1, we compare the evolution of the Taylor microscale Reynolds number, Re_λ , with other Reynolds numbers: Re_{k_f} and Re_t , whose values at $t = t_*$ are given in Table 1 for $k_f/k_1 = 10$, and the maximum of Re_k over k , $max_k(Re_k)$, which is at later times dominated by the peak at small k ; see Figure 9, where the peak is at $k/k_1 \approx 2$. Note that $max_k(Re_k)$ begins to grow exponentially shortly after $t c_s k_1 \approx 1.1$.

In Sect. 5, we compared our critical magnetic Reynolds number of 25 with the earlier value of 35 by Haugen et al. (2004b), and we argued that the new value is smaller because of helicity in the flow. We also stated that the results depend on the Mach number (Haugen et al. 2004b). We can now compare with the highly compressible, supersonic hydromagnetic turbulence simulations of Federrath et al. (2014), who gave a critical magnetic Reynolds number of ≈ 130 . This value is based on half the size of the computational domain. To convert it to the normalization of Haugen et al. (2004a,b), it should be divided by 2π . This results in a value of ≈ 20 , which is smaller than the values of 35 to 70 found by Haugen et al. (2004b) for Mach numbers below and above unity, respectively. However, when they increased their magnetic Prandtl number from unity to five, they found $Re_M^{\text{crit}} = 25$ and 50 for Mach numbers below and above unity, respectively; compare Figs. 7 and 8 of Haugen et al. (2004b). Federrath et al. (2014) used $Pr_M = 10$, so their value of $Re_M^{\text{crit}} = 20$ cannot directly be compared with those of Haugen et al. (2004b) for $Pr_M = 5$, but it seems a bit low. This question cannot be fully clarified here and might depend on subtle numerical aspects. The FLASH code (Fryxell et al. 2000) used by Federrath et al.

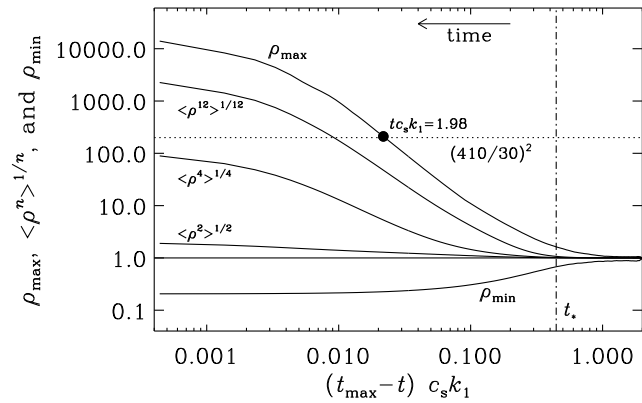


Figure D1. Evolution of the maximum density along with the minimum density and intermediate moments of the density for $n = 2, 4$, and 12 . Note that time increases toward the left. The time $t_{c_s k_1} = 1.98$ for which the Jeans length becomes resolved by less than 30 mesh points is marked by the black symbol. This is when $(\rho_{\max}/\rho_0)^{1/2} = 410/30$.

(2014) is based on a Riemann solver, which may affect the effective viscosity and magnetic diffusivity.

APPENDIX D: MAXIMUM DENSITY AND OTHER DENSITY MOMENTS

As time goes on and the collapse proceeds, the density contrast increases. This has implications for the nominal Jeans length, which decreases with increasing maximum density. To get an idea of this, we plot in Figure D1 the evolution of the maximum density. For completeness, we also plot the minimum density and intermediate moments of the density, $\langle \rho^n \rangle^{1/n}$ for $n = 2, 4$, and 12 . Note that

$$\rho_{\max} = \lim_{n \rightarrow \infty} \langle \rho^n \rangle^{1/n}, \quad \text{and} \quad \rho_{\min} = \lim_{n \rightarrow -\infty} \langle \rho^n \rangle^{1/n}. \quad (\text{D1})$$

To show the values close to the collapse time t_{\max} more clearly, we plot the densities versus $(t_{\max} - t) c_s k_1$ in a doubly-logarithmic representation.

The nominal Jeans length is proportional to $\rho^{-1/2}$, although the standard stability analysis breaks down if the density is no longer constant. We see that the resolution criterion of Federrath et al. (2011b) is reached when the square root of the density exceeds $1/30$ of the initial Jeans length of 410 grid cells for $\sigma_J/c_s k_1 = 5$; see Sect. 2.3.

REFERENCES

Alecian G., Leorat J., 1988, *A&A*, **196**, 1
 André P., Belloche A., Motte F., Peretto N., 2007, *A&A*, **472**, 519
 Banerjee S., Kritsuk A. G., 2018, *PhRvE*, **97**, 023107
 Barreto-Mota L., de Gouveia Dal Pino E. M., Burkhardt B., Melioli C., Santos-Lima R., Kadowaki L. H. S., 2021, *MNRAS*, **503**, 5425
 Berger M. A., 1997, *J. Geophys. Res.*, **102**, 2637
 Binney J., Tremaine S., 2008, *Galactic Dynamics: Second Edition*
 Bonazzola S., Heyvaerts J., Falgarone E., Perault M., Puget J. L., 1987, *A&A*, **172**, 293
 Bournaud F., Elmegreen B. G., Teyssier R., Block D. L., Puerari I., 2010, *MNRAS*, **409**, 1088

Brandenburg A., 2009, *ApJ*, **697**, 1206
 Brandenburg A., Matthaues W. H., 2004, *PhRvE*, **69**, 056407
 Brandenburg A., Kahniashvili T., Mandal S., Roper Pol A., Tevzadze A. G., Vachaspati T., 2019, *PhRvF*, **4**, 024608
 Brandenburg A., Durrer R., Huang Y., Kahniashvili T., Mandal S., Mukohyama S., 2020, *PhRvD*, **102**, 023536
 Chen C.-Y., King P. K., Li Z.-Y., 2016, *ApJ*, **829**, 84
 Crutcher R. M., 1999, *ApJ*, **520**, 706
 Crutcher R. M., 2012, *ARA&A*, **50**, 29
 Dekel A., et al., 2009, *Natur*, **457**, 451
 Elperin T., Kleeorin N., Rogachevskii I., 2003, *PhRvE*, **68**, 016311
 Falco M., Hansen S. H., Wojtak R., Mamon G. A., 2013, *MNRAS*, **431**, L6
 Federrath C., Klessen R. S., 2012, *ApJ*, **761**, 156
 Federrath C., Banerjee R., Clark P. C., Klessen R. S., 2010, *ApJ*, **713**, 269
 Federrath C., Chabrier G., Schober J., Banerjee R., Klessen R. S., Schleicher D. R. G., 2011a, *PhRvL*, **107**, 114504
 Federrath C., Sur S., Schleicher D. R. G., Banerjee R., Klessen R. S., 2011b, *ApJ*, **731**, 62
 Federrath C., Schober J., Bovino S., Schleicher D. R. G., 2014, *ApJL*, **797**, L19
 Federrath C., Klessen R. S., Iapichino L., Beattie J. R., 2021, *Nature Astronomy*, **5**, 365
 Field G. B., Blackman E. G., Keto E. R., 2008, *MNRAS*, **385**, 181
 Fryxell B., et al., 2000, *ApJS*, **131**, 273
 Haugen N. E. L., Brandenburg A., Dobler W., 2003, *ApJL*, **597**, L141
 Haugen N. E., Brandenburg A., Dobler W., 2004a, *PhRvE*, **70**, 016308
 Haugen N. E. L., Brandenburg A., Mee A. J., 2004b, *MNRAS*, **353**, 947
 Hennebelle P., Falgarone E., 2012, *A&AR*, **20**, 55
 Hide R., Palmer T. N., 1982, *Geophysical and Astrophysical Fluid Dynamics*, **19**, 301
 Ibáñez-Mejía J. C., Mac Low M.-M., Klessen R. S., Baczynski C., 2017, *ApJ*, **850**, 62
 Jeans J. H., 1902, *RSPTA*, **199**, 1
 Johansen A., Oishi J. S., Mac Low M.-M., Klahr H., Henning T., Youdin A., 2007, *Natur*, **448**, 1022
 Käpylä P. J., Mitra D., Brandenburg A., 2009, *PhRvE*, **79**, 016302
 Karoly J., Soam A., Andersson B. G., Coudé S., Bastien P., Vailancourt J. E., Lee C. W., 2020, *ApJ*, **900**, 181
 Klessen R. S., Hennebelle P., 2010, *A&A*, **520**, A17
 Krumholz M. R., Burkhardt B., 2016, *MNRAS*, **458**, 1671
 Krumholz M. R., Burkhardt B., Forbes J. C., Crocker R. M., 2018, *MNRAS*, **477**, 2716
 Lane H. B., Grudić M. Y., Guszejnov D., Offner S. S. R., Faucher-Giguère C.-A., Rosen A. L., 2022, *MNRAS*, **510**, 4767
 Larson R. B., 1981, *MNRAS*, **194**, 809
 Lee Y.-N., Hennebelle P., 2018, *A&A*, **611**, A89
 Mac Low M.-M., Klessen R. S., 2004, *Reviews of Modern Physics*, **76**, 125
 Mattsson L., Hedvall R., 2022, *MNRAS*, **509**, 3660
 Mee A. J., Brandenburg A., 2006, *MNRAS*, **370**, 415
 Mestel L., Spitzer L. J., 1956, *MNRAS*, **116**, 503
 Moffatt H. K., 1978, *Magnetic Field Generation in Electrically Conducting Fluids*. Cambridge University Press, Cambridge
 Mouschovias T. C., Spitzer L. J., 1976, *ApJ*, **210**, 326
 Myers P. C., Ladd E. F., Fuller G. A., 1991, *ApJL*, **372**, L95
 Nelson D., Genel S., Vogelsberger M., Springel V., Sijacki D., Torrey P., Hernquist L., 2015, *MNRAS*, **448**, 59
 Nordlund A., Brandenburg A., Jennings R. L., Rieutord M., Ruokolainen J., Stein R. F., Tuominen I., 1992, *ApJ*, **392**, 647
 Ntormousi E., Hennebelle P., 2019, *A&A*, **625**, A82
 Passot T., Vazquez-Semadeni E., Pouquet A., 1995, *ApJ*, **455**, 536
 Pattle K., et al., 2021, *ApJ*, **907**, 88
 Pencil Code Collaboration et al., 2021, *JOSS*, **6**, 2807

- Porter D. H., Jones T. W., Ryu D., 2015, [ApJ](#), **810**, 93
- Pudritz R. E., Rogers C. S., Ouyed R., 2006, [MNRAS](#), **365**, 1131
- Roper Pol A., Mandal S., Brandenburg A., Kahniashvili T., Kosowsky A., 2020, [PhRvD](#), **102**, 083512
- Schneider N., et al., 2013, [ApJL](#), **766**, L17
- Sharda P., Federrath C., Krumholz M. R., Schleicher D. R. G., 2021, [MNRAS](#), **503**, 2014
- Shu F. H., 1977, [ApJ](#), **214**, 488
- Shu F. H., 1992, *The physics of astrophysics. Volume II: Gas dynamics.*
- Soler J. D., Hennebelle P., 2017, [A&A](#), **607**, A2
- Soler J. D., Hennebelle P., Martin P. G., Miville-Deschênes M. A., Netterfield C. B., Fissel L. M., 2013, [ApJ](#), **774**, 128
- Sur S., 2019, [MNRAS](#), **488**, 3439
- Sur S., Schleicher D. R. G., Banerjee R., Federrath C., Klessen R. S., 2010, [ApJL](#), **721**, L134
- Sur S., Federrath C., Schleicher D. R. G., Banerjee R., Klessen R. S., 2012, [MNRAS](#), **423**, 3148
- Tennekes H., Lumley J. L., 1972, *First Course in Turbulence*
- Truelove J. K., Klein R. I., McKee C. F., Holliman John H. I., Howell L. H., Greenough J. A., 1997, [ApJL](#), **489**, L179
- Xu S., Lazarian A., 2020, [ApJ](#), **899**, 115